New constraints on anisotropic expansion from supernovae Type Ia

W. Rahman,[1]★ R. Trotta,[1,2,3]★ S. S. Boruah,[4] M. J. Hudson [5,6,7] and D. A. van Dyk[2,8]

[1]*Astrophysics Group, Physics Department, Blackett Laboratory, Imperial College London, Prince Consort Rd, London SW7 2AZ, UK*
[2]*Data Science Institute, William Penney Laboratory, Imperial College London, London SW7 2AZ, UK*
[3]*International School for Advanced Studies (SISSA), Theoretical and Scientific Data Science Group, Physics Department, Via Bonomea 265, I-34136 Trieste, Italy*
[4]*Department of Astronomy and Steward Observatory, University of Arizona, 933 N Cherry Ave, Tucson, AZ 85719, USA*
[5]*Department of Physics and Astronomy, University of Waterloo, Waterloo, ON N2L 3G1, Canada*
[6]*Waterloo Centre for Astrophysics, Waterloo, ON N2L 3G1, Canada*
[7]*Perimeter Institute for Theoretical Physics, 31 Caroline St. N., Waterloo, ON N2L 2Y5, Canada*
[8]*Statistics Section, Mathematics Department, Imperial College London, Huxley Building, Queen's Gate, London SW7 2AZ, UK*

ABSTRACT

We re-examine the contentious question of constraints on anisotropic expansion from Type Ia supernovae (SNIa) in the light of a novel determination of peculiar velocities, which are crucial to test isotropy with SNe out to distances $\gtrsim 200\,h^{-1}$ Mpc. We re-analyse the Joint Light-Curve Analysis (JLA) Supernovae (SNe) data, improving on previous treatments of peculiar velocity corrections and their uncertainties (both statistical and systematic) by adopting state-of-the-art flow models constrained independently via the 2M++ galaxy redshift compilation. We also introduce a novel procedure to account for colour-based selection effects, and adjust the redshift of low-z SNe self-consistently in the light of our improved peculiar velocity model. We adopt the Bayesian hierarchical model BAHAMAS to constrain a dipole in the distance modulus in the context of the Lambda cold dark matter (ΛCDM) model and the deceleration parameter in a phenomenological Cosmographic expansion. We do not find any evidence for anisotropic expansion, and place a tight upper bound on the amplitude of a dipole, $|D_\mu| < 5.93 \times 10^{-4}$ (95 per cent credible interval) in a ΛCDM setting, and $|D_{q_0}| < 6.29 \times 10^{-2}$ in the Cosmographic expansion approach. Using Bayesian model comparison, we obtain posterior odds in excess of 900:1 (640:1) against a constant-in-redshift dipole for ΛCDM (the Cosmographic expansion). In the isotropic case, an accelerating universe is favoured with odds of $\sim$1100:1 with respect to a decelerating one.

Key words: methods: statistical – supernovae: general – cosmological parameters – cosmology: observations – dark energy.

1 INTRODUCTION

A fundamental assumption underpinning the cosmological concordance model is the cosmological principle, namely that the universe is homogeneous and isotropic on sufficiently large scales. Given the ubiquity of the cosmological principle, an observational test of this assumption is an important step towards validating our best description of the large-scale universe. Testing of homogeneity is hampered by the need of surveying extremely large scales (see Maartens 2011), although recent studies have found the transition to homogeneity at high ($z \sim 2$) redshift consistent with expectations from the Lambda cold dark matter (ΛCDM) cosmological concordance model (Gonçalves et al. 2018, 2021).

The assumption of isotropy has been tested over a range of redshifts and with many different probes, from the relatively local universe out to the redshift of recombination. Analyses of Cosmic Microwave Background (CMB) anisotropies data obtained by the Wilkinson Microwave Anisotropy Probe (WMAP) and the Planck satellite found

up to $\sim$3σ evidence of breaches of statistical isotropy in the form of power asymmetry between hemispheres, multipole alignments, anomalous clustering of directions, although the significance of these results is difficult to assess, partially because of issues of *a posteriori* testing (Bennett et al. 2013; Akrami et al. 2014; Planck Collaboration XVI 2016; Schwarz et al. 2016). Quasar polarization directions also appear to be aligned along anomalous directions in the CMB (Hutsemékers et al. 2005) and with coherence scales in excess of 500 Mpc (Hutsemékers et al. 2014), in potential disagreement with the cosmological principle. Investigating the distribution of galaxies on large scales, Sarkar, Pandey & Khatri (2019) found however good agreement between the predictions of ΛCDM and the *Sloan Digital Sky Survey* data, with a transition to isotropy observed beyond a length-scale of $200\,h^{-1}$ Mpc (where h is the dimensionless Hubble-Lemaître parameter). More recently, Secrest et al. (2020) reported a one-sided 4.9σ rejection of the hypothesis that the dipole in a sample of 1.3 million quasars is purely due to our motion with respect to the CMB.

Supernovae Type Ia (SNIa) can be used to test the second expression of the cosmological principle, namely that the expansion of the universe is isotropic. SNIa are a sub-class of supernovae (SNe),

★ E-mail: rahmanw@hotmail.co.uk (WR); rtrotta@sissa.it (RT)

resulting from the thermonuclear explosion of CO white dwarfs accreting mass near the Chandrasekhar limit, whose spectra exhibit no hydrogen lines but strong silicon lines. A series of corrections can be applied to account for correlations of absolute peak magnitude with their light curve decline rate and colour. The correlation with light curve decline rate were first observed by Rust (1974) and further corroborated later by Pskovskii (1977, 1984) and Phillips (1993) using larger samples of SNe type Ia. Later a correlation with colour was also observed and it was noticed that brighter SNIa had a bluer colour (Hamuy et al. 1995; Riess, Press & Kirshner 1996; Perlmutter et al. 1997). Empirical corrections that account for correlations of absolute peak magnitude with their decline time and colour can then be applied to standardize the SNIa data (Tripp 1998; Phillips et al. 1999). Light curves of SNe type Ia can be standardized so that the residual scatter of their peak *B*-band magnitude is sufficiently small (∼0.1 mag) to infer cosmological parameters, as was first demonstrated by Riess et al. (1998) and Perlmutter et al. (1999). SNe type Ia observations can also be used to test the hypothesis of isotropy in the expansion of the universe underpinning the Friedemann–Lemaître–Robertson–Walker (FLRW) metric of the concordance cosmological model, which exhibits an isotropic scale factor $a(t)$. To this end, various authors have analysed increasingly large SNIa compilations with different statistical approaches, often with sharply discordant results.

After early works (Kolatt & Lahav 2001; Schwarz & Weinhorst 2007; Gupta, Saini & Laskar 2008), Cooke & Lynden-Bell (2010) analysed a subset of 250 SNIa from the Union compilation (Kowalski et al. 2008) with $z > 0.2$ with a maximum likelihood approach to constrain a dipolar modulation to the luminosity distance, finding no significant deviation from isotropy. However, Cai & Tuo (2012) claimed that the deceleration parameter shows a preferred direction in the Union2 (Amanullah et al. 2010) compilation of 557 SNIa, a result corroborated by the analysis of Antoniou & Perivolaropoulos (2010), who combined SNIa data with other cosmological probes. Jiménez, Salzano & Lazkoz (2015) analysed the same Union2 data, additionally including the SNLS3 data, and showed that previous claims of anisotropy disappear if one accounts for correlations among the observations by including the full data covariance matrix in the analysis. Other null results of anisotropic expansion include Heneka, Marra & Amendola (2014) and Lin et al. (2016a), who investigated the Joint Light-curve Analysis (JLA) compilation (Betoule et al. 2014) of 740 SNIa [see also Sun & Wang (2019), who obtain discrepant results from three different compilations of SNIa namely Union 2.1, JLA and Constitution (Hicken et al. 2009)]. Similarly Andrade et al. (2018a), find the JLA data prefers isotropy, with the results being inconclusive on the Union2.1 data. Javanmardi et al. (2015) however, find that the null hypothesis of isotropy cannot be rejected unless ones specifically takes into account its alignment with the dipole of the Cosmic Microwave Background (CMB), in which case the null hypothesis can be rejected at a level ranging from 95 to 99 per cent confidence. An important distinction between these data sets is that Union2/2.1 and Constitution have no corrections for the peculiar velocities of the SNe host galaxies, whereas JLA does. Bernal, Cárdenas & Motta (2017) found from Union2 and LOSS data potential differences between hemispheres in the isotropy of the deceleration parameter.

The situation becomes more confused when considering the largest SNIa compilation to date, Pantheon, encompassing 1048 objects in the redshift range $0.01 < z < 2.3$ (Scolnic et al. 2018b). A major hurdle to any re-analysis that uses Pantheon is the lack of a publicly available full correlation matrix for its SNIa light-curve standardization coefficients, which hampers a principled statistical approach.

Nevertheless, several papers have attempted to use Pantheon-derived measurements of the distance modulus as a function of redshift to investigate potential deviations from an isotropic expansion, finding isotropy is still favoured (Andrade et al. 2018b; Sun & Wang 2018b; Soltis et al. 2019; Zhao, Zhou & Chang 2019).

Despite the existence of substantially larger compilations like Pantheon, the JLA remains a useful data set for analyses of this kind, because all the necessary statistical and systematics covariance matrixes are publicly available, unlike e.g. the Pantheon set. Recently, Colin et al. (2019b) (henceforth C19) claimed 3.9σ evidence for a dipole in the deceleration parameter from a maximum likelihood analysis of JLA data, leading to a lack of statistical evidence for acceleration in the expansion. The claim was disputed by Rubin & Heitlauf (2020) (henceforth, RH20), who pointed out the incorrect use of heliocentric redshifts in C19 and other technical assumptions about selection effects which, when corrected, remove the preference for a dipole and restore the high significance for an accelerated expansion [see also the discussion in Rubin & Hayden (2016), itself a rebuttal of Nielsen, Guffanti & Sarkar (2016).] A further reply by Colin et al. (2019a) appears to concede some technical points, but not the overall conclusion on the actual lack of statistical significance for an accelerated expansion.

The aim of this work is to clarify the status of claims for a statistically significant dipole in the accelerated expansion of the universe, especially in light of the ongoing controversy. In so doing, we also revisit the important question of the level of statistical evidence in favour of the accelerated expansion in an isotropic universe from SNIa data alone. We address the criticisms of the published JLA data made by C19, who claimed that the peculiar velocity corrections made to the JLA SNIa data based on local bulk flows are incorrect. In this paper, we introduce a state-of-the-art treatment of peculiar velocities, which are independently constrained using the 2M++ galaxy catalogue (Lavaux & Hudson 2011; Boruah, Hudson & Lavaux 2020, 2021), re-derive correlated peculiar velocity uncertainties (both statistical and systematic) from a fully consistent flow model, and upgrade the Bayesian hierarchical model BAHAMAS Shariff et al. (2016) to include an new treatment of residual colour-based selection effects in SNIa data.

The remaining of this paper is structured as follows: Section 2 introduces the cosmological model, the anisotropy model, our Bayesian framework, the data used, our new peculiar velocities treatment and our new colour-based selection effects correction. Section 3 demonstrates the performance of our method on simulated data. Our results from the JLA data, both in terms of parameter inference and Bayesian model comparison, are presented in Section 4. Our conclusions are given in Section 5.

2 METHODOLOGY AND DATA

2.1 Cosmological model and dipole modulation

We investigate the isotropy of the expansion in both a model-specific and a model-independent way: first, we consider the ΛCDM model for the underlying cosmology; secondly, we use the so-called 'Cosmographic expansion' (i.e. a Taylor expansion of the scale factor as a function in time) as a model-independent description of the underlying matter-energy density of the universe.

The ΛCDM model has cosmological parameters $\mathscr{P}_1 = \{\Omega_m, \Omega_\Lambda, H_0\}$, where Ω_m and Ω_Λ are the density parameters of matter (both baryonic and dark) and cosmological constant, Λ, respectively, in units of the critical energy density; H_0 is the Hubble–Lemaître constant (which we fix to $H_0 = 72$ km s^{-1} Mpc^{-1}, as it is

exactly degenerate with the SNIa intrinsic magnitude). The curvature parameter Ω_κ is given by

$$\Omega_\kappa = 1 - \Omega_m - \Omega_\Lambda \tag{1}$$

and we assume a universe with constant dark energy equation of state, $w(z) = -1$. We denote by $\bar{z}$ the redshift of a comoving galaxy seen by an observer who is also at rest w.r.t. to the CMB restframe (i.e. the 'cosmological' redshift, with no peculiar velocities from either the source or the observer) and by z_{hel} redshift for an observer in the Sun's frame of reference.[1] The measured redshift in our heliocentric frame of reference is given by $\hat{z}_{\text{hel}}$, and it differs from z_{hel} by measurement noise. The redshift in our heliocentric frame of reference, z_{hel}, differs from the redshift of a comoving observer, $\bar{z}$, by virtue of peculiar velocities of the source and the observer, and gravitational red/blueshifts due to the local gravitational potential at the location of the source and observer. In the following, we neglect gravitational effects, which are subdominant (see however Calcino & Davis [2017]) and focus instead on the impact of peculiar velocities.

The relationship between heliocentric redshift, z_{hel}, and the redshift of a comoving galaxy as seen by an observer at rest w.r.t. the CMB, $\bar{z}$ is given by

$$(1 + z_{\text{hel}}) = (1 + z_{\text{CMB}})(1 + z_{\text{pec}}^\odot) \tag{2}$$

$$(1 + z_{\text{CMB}}) = (1 + \bar{z})(1 + z_{\text{pec}}^{\text{SN}}), \tag{3}$$

where $z_{\text{pec}}^\odot$ is the redshift induced by the peculiar velocity of the Solar system w.r.t. the CMB rest frame, while $z_{\text{pec}}^{\text{SN}}$ is the redshift caused by the peculiar velocity of the SNIa w.r.t. the CMB frame. The second equality introduces the redshift in the CMB rest frame, z_{CMB}, i.e. the frame in which our motion w.r.t. the CMB has been removed.[2] With the above definitions, we can write the luminosity distance to redshift $\bar{z}$, as (Davis et al. [2011])

$$d_L\left(\bar{z}, z_{\text{pec}}^\odot, z_{\text{pec}}^{\text{SN}}, \mathscr{P}_1\right) = \frac{c}{H_0} \frac{(1 + \bar{z})(1 + z_{\text{pec}}^\odot)(1 + z_{\text{pec}}^{\text{SN}})^2}{\sqrt{|\Omega_\kappa|}}$$
$$\times \text{sinn}\left\{\sqrt{|\Omega_\kappa|} \int_0^{\bar{z}} \frac{dz}{E(z)}\right\}. \tag{4}$$

$E(z)$ depends on our choice of cosmology and for the ΛCDM universe, is given by

$$E^2(z) = \Omega_M(1 + z)^3 + \Omega_\Lambda + \Omega_\kappa(1 + z)^2. \tag{5}$$

The $\text{sinn}(x)$ function is defined as

$$\text{sinn}(x) = \begin{cases} x & \text{if } \Omega_\kappa = 0 \\ \sin(x) & \text{if } \Omega_\kappa < 0 \\ \sinh(x) & \text{if } \Omega_\kappa > 0 \end{cases}. \tag{6}$$

In our model-independent approach, we follow Visser ([2004]) and Taylor-expand the scale factor of the FLRW metric up to third order

in time around t_0 (today), as

$$a(t) = a_0\left\{1 + H_0(t - t_0) - \frac{1}{2}q_0 H_0^2(t - t_0)^2 + \frac{1}{3!}j_0 H_0^3(t - t_0)^3\right.$$
$$\left. + O([t - t_0]^4)\right\}, \tag{7}$$

where q_0 is the dimensionless deceleration parameter, defined as

$$q_0 = -\frac{1}{a}\frac{d^2 a}{dt^2}\left[\frac{1}{a}\frac{da}{dt}\right]^{-2}_{t=t_0} \tag{8}$$

and j_0 is the so-called 'jerk',

$$j_0 = +\frac{1}{a}\frac{d^3 a}{dt^3}\left[\frac{1}{a}\frac{da}{dt}\right]^{-3}_{t=t_0}, \tag{9}$$

which is also dimensionless. This model-independent expansion only relies on the FLRW metric but makes no assumption about the underlying matter-energy density, and leads to the following form of the luminosity distance at redshift $\bar{z}$:

$$d_L\left(\bar{z}, z_{\text{pec}}^\odot, z_{\text{pec}}^{\text{SN}}, \mathscr{P}_2\right) = \frac{(1 + z_{\text{pec}}^\odot)(1 + z_{\text{pec}}^{\text{SN}})^2}{1 + \bar{z}}\frac{c\bar{z}}{H_0}\left[1 + \frac{1}{2}(1 - q_0)\bar{z}\right.$$
$$\left. - \frac{1}{6}(1 - q_0 - 3q_0^2 + j_0 - \Omega_\kappa)\bar{z}^2 + O(\bar{z}^3)\right], \tag{10}$$

where c is the speed of light and the model-independent parameters are $\mathscr{P}_2 = \{H_0, q_0, j_0, \Omega_\kappa\}$. From expressions ([4]) or ([10]), we obtain the isotropic distance modulus, μ_I, using the standard formula

$$\mu_I\left(\bar{z}, z_{\text{pec}}^\odot, z_{\text{pec}}^{\text{SN}}, \mathscr{P}_a\right) = 25 + 5\log_{10}\frac{d_L\left(\bar{z}, z_{\text{pec}}^\odot, z_{\text{pec}}^{\text{SN}}, \mathscr{P}_a\right)}{1 \text{ Mpc}}, \tag{11}$$

where $a = 1, 2$ depending on the chosen parametrization.

There are several different ways one can parametrize the possibility of anisotropic expansion, depending on the underlying physical origin for the effect. A spherical harmonics expansion introduces, to lowest order, a dipolar modulation in the direction of a SNIa situated at redshift $\bar{z}$ and in direction $\mathbf{n}_{\text{SN}}$ in the sky, with $\mathbf{n}_{\text{SN}}$ a unit vector pointing from the centre of the coordinate system (the Earth) to the location of the SNIa on the celestial sphere. Different authors have taken different approaches in the literature, with no consensus as to which quantity should be modulated: one could expand the scale factor $a(t)$, the luminosity distance, the comoving distance, the Hubble parameter, the matter density, the cosmological constant density, or the distance modulus. Each of these possibilities leads to a different anisotropic imprint on to the Hubble–Lemaître law. A dipole moment that is constant with distance, r, in the peculiar velocity field (i.e. a bulk flow) leads to

$$c\bar{z} \approx H_0 r + D_v(\mathbf{n}_{\text{dip}} \cdot \mathbf{n}_{\text{SN}}). \tag{12}$$

By contrast, a constant dipole in either H_0 or r leads to

$$c\bar{z} \approx H_0 r + H_0 D_H r(\mathbf{n}_{\text{dip}} \cdot \mathbf{n}_{\text{SN}}), \tag{13}$$

which increases linearly with distance. Another possibility is to modulate the distance modulus directly:

$$\mu = \mu_I(\bar{z}, z_{\text{hel}}, \mathscr{P}_a)\left(1 + D_\mu F(\bar{z})(\mathbf{n}_{\text{dip}} \cdot \mathbf{n}_{\text{SN}})\right), \tag{14}$$

where $F(z)$ is a function of redshift alone which can be used to localize the dipole at a given length-scale. Yet another approach, adopted by C19, is to model the dipole on the deceleration parameter, q_0, in a Cosmographic expansion:

$$q_0(z) = q_m + D_{q_0} F(\bar{z})(\mathbf{n}_{\text{dip}} \cdot \mathbf{n}_{\text{SN}}). \tag{15}$$

---

[1]We neglect the distinction between geocentric and heliocentric frames of references (the difference due to the ~30 km s^{-1} orbital speed of the Earth is of order $\Delta z \sim 10^{-5}$), since redshift measurements are routinely reported in the heliocentric frame and also already corrected for atmospheric refraction.
[2]A source of confusion in the literature is the widespread use of the term 'CMB rest frame' to denote what we call $\bar{z}$ (i.e. the cosmological redshift, with no peculiar motions from either source nor observer). This misleading nomenclature is for example used by Betoule et al. ([2014]), as well as in the data products of the JLA data release.

In this paper, we add the dipole to either the distance modulus, equation (14), or to the deceleration parameter, equation (15), and consider both $F(z) = 1$ and, following C19, an exponentially decaying function of redshift with characteristic scale given by the free parameter S, namely $F(z) = \exp(-z/S)$. These two forms have the effect of either creating a dipole that is constant in redshift or constrained to a local scale which could arise for reasons such as existing within a cosmic void.

As noted in previous works, a phenomenological approach as the one taken here that perturbs an underlying FLRW metric may not be entirely consistent. An alternative route would require specifying a physical model for the anisotropy, and then derive the ensuing predictions for the distance modulus and compare those with observations, as done for example in the context of an ellipsoidal universe from Bianchi type I models (Campanelli et al. 2011). However, the advantage of a purely phenomenological approach is that it remains agnostic about the underlying cause of any anisotropy, and it provides constraints on the level of anisotropy that can then be applied to other models.

2.2 Bayesian Hierarchical Model

In this paper, we improve on previous works constraining anisotropy from SNe data by adopting a fully Bayesian hierarchical model (BHM) for the statistical analysis of SNIa data, called BAHAMAS. 'Hierarchical' here refers to the existence, within the model, of a layer of unobserved (so-called 'latent') variables for each SNIa, corresponding to the true value of their light curve-derived properties (as opposed to the noisy measured value). The latent variables are marginalized over in the inference, and are constrained in virtue of the fact that they are all generated from the same underlying population distribution, which is modelled with a set of hyperparameters, themselves determined from the data. This approach has been shown to have better coverage statistics overall than the χ^2 method traditionally employed, and leads to a reduction of mean squared errors for the recovered cosmological parameters by a factor of ∼2–3 when deployed on simulated data (March et al. 2011; Shariff et al. 2016). Furthermore, the BAHAMAS framework can be used for principled Bayesian model comparison of the kind we perform in Section 4.2, as it correctly marginalizes out all nuisance parameters. By contrast, the heuristic χ^2 approach traditionally adopted is an approximation to the BAHAMAS likelihood, and cannot be used to compute Bayes factors or for formal Bayesian model comparison.

The Bayesian methodology pioneered in March et al. (2011) has been adopted and extended in several other papers, including e.g. UNITY (Rubin et al. 2015), STEVE (Hinton et al. 2018), and Simple-BayeSN (Mandel et al. 2017). (See also Nielsen et al. (2016) for a profile likelihood interpretation.) Here, we briefly summarize our Bayesian Hierarchical model, which builds on BAHAMAS, referring the reader to March et al. (2011) and Shariff et al. (2016) for fuller details.

We denote with a hat symbol observed quantities, in order to distinguish them from the latent (i.e. unobserved) variables in our model. For each SNIa i, the data d_i can be summarized by a vector

$$d_i = \{\hat{z}_{\text{hel},i}, \hat{c}_i, \hat{x}_{1_i}, \hat{m}_{B_i}, \hat{\Sigma}_{C,i}\}, \tag{16}$$

where $\hat{z}_{\text{hel},i}$ is the observed heliocentric redshift, $\hat{m}_{B_i}$ is the observed peak B-band apparent magnitude, $\hat{x}_{1_i}$ and $\hat{c}_i$ are observed 'stretch' and 'colour' corrections, which are summary statistics of the light curve of the SNIa obtained with the light curve fitter SALT2 (Guy et al. 2005, 2007) during the standardization procedure. Furthermore, $\hat{\Sigma}_{C,i} = \text{Cov}(\hat{c}_i, \hat{x}_{1_i}, \hat{m}_{B_i})$ is a 3×3 variance-covariance matrix that

describes the measurement error on the observables. On the standard deviation scale, the measurement error for redshift for SNIa with spectroscopic follow-up is $\sigma_z^{\text{spSN}} \sim 5 \times 10^{-3}$ when the redshift is determined from the SNIa spectrum alone, and $\sigma_z^{\text{spHost}} \sim 5 \times 10^{-4}$ when it is obtained from host-galaxy spectra (Zheng et al. 2008). The redshift measurements are independent from each other and from all other observables. We discuss this uncertainty further in Section 2.6. (See also Calcino & Davis (2017) for the potentially important impact of systematic redshift errors as small as $\Delta z \sim 10^{-4}$.)

In BAHAMAS, we introduce latent variables for each SNIa in order to model each source of uncertainty according to its origin: measurement error, population scatter, and intrinsic (residual) variability. A probabilistic hierarchical model is built as follows: each SNIa has latent variables M_i^ϵ, x_{1_i}, and c_i, representing the objects' 'true' (i.e. noiseless) absolute magnitude, stretch correction, and colour correction, respectively. These latent variables follow normal distributions, representing population variability of the SNe and parametrized by their means and variances:

$$x_{1_i} \sim \mathcal{N}\left(x_{1\star}, R_{x_1}^2\right), \tag{17}$$

$$c_i \sim \mathcal{N}\left(c_\star, R_c^2\right), \tag{18}$$

$$M_i^\epsilon \sim \mathcal{N}\left(M_0^\epsilon, \sigma_{\text{res}}^2\right), \tag{19}$$

where $x_{1\star}$, $c_\star$, and M_0^ϵ are the population means and $R_{x_1}^2$, R_c^2, and σ_{res}^2 are the population variances, all of which are also estimated from the data. We collect the population-level parameters in a vector of variables $\vartheta \equiv \{x_{1\star}, c_\star, M_0^\epsilon, R_{x_1}^2, R_c^2, \sigma_{\text{res}}^2\}$. The intrinsic magnitude of each SNIa M_i, is modified by applying the linear 'Tripp relation' (Tripp 1998), so that $M_i \rightarrow M_i^\epsilon \equiv M_i + \alpha x_{1_i} - \beta c_i$, where α and β are nuisance parameters that control the slope of the stretch and colour correction, respectively. Therefore, M_i^ϵ is a linear function of M_i that features a lower population variance, represented by σ_{res}^2. In astrophysical parlance, M_i^ϵ is referred to as 'the corrected intrinsic magnitude' of the SNIa. Thanks to the standardization procedure, the residual standard deviation of the SNe type Ia's corrected intrinsic magnitude can be sufficiently reduced so that they can be used as luminosity distance indicators. Shariff et al. (2016) used the BAHAMAS model to determine the residual standard deviation of the corrected intrinsic magnitude, finding (from JLA data) a value $\sigma_{\text{res}} \sim 0.104 \pm 0.005$, similar to (if somewhat smaller than) the value obtained with a χ^2 method by Betoule et al. (2014). At the latent level, the apparent peak magnitude m_{B_i} is related to the standardized intrinsic magnitude M_i^ϵ via the isotropic distance modulus of equation (11):

$$m_{B_i} = \mu_I(z_{\text{hel},i}, \bar{z}_{,i}, \mathscr{P}_a) - \alpha x_{1_i} + \beta c_i + M_i^\epsilon. \tag{20}$$

Finally, the observed values of $\{\hat{m}_{B_i}, \hat{x}_{1_i}, \hat{c}_i\}$ are modelled as normally distributed around their latent values, with variance-covariance matrix given by $\hat{\Sigma}_{C,i}$. Additionally, a systematic errors covariance matrix that correlates different SNIe (for example, because of calibration uncertainties common between SNIe within the same survey) is included when available. Inference is based on the marginal distribution of the quantities of interest, $\mathscr{P}_a$, which includes uncertainty at all levels of the hierarchy.

It has become common practice to split the SNe into two groups, based on their host-galaxy stellar mass (Sullivan et al. 2010), with the mass threshold between the two groups being around value of $\log_{10}(M_g) = 10$, where M_g is the host-galaxy mass measured in solar masses. Smith et al. (2020) found a difference of up to 0.04 mag in the average intrinsic magnitude of the two groups, and application

of the Tripp relation to the two groups separately may further reduce the residual dispersion in SNIa absolute magnitudes. (See also Thorp et al. (2021) for a similar result obtained using a Bayesian hierarchical approach.) However, Brout & Scolnic (2021) have recently cast doubt on the robustness of this mass-step correction, which they ascribed instead to incorrect dust modelling. The ultimate origin of the mass step remains unclear, and it might relate to stellar population age (Childress, Wolf & Zahid 2014) and metallicity (Sullivan et al. 2010). In any case, Shariff et al. (2016) showed that adding a mass-step or a more general linear covariate as a function of host-galaxy mass has little impact on the ensuing cosmological parameters inference. Therefore, in this paper we do not adopt a mass-step correction. We refer the reader to March et al. (2011) and Shariff et al. (2016) for the full mathematical detail of the BAHAMAS model, marginalization procedure and algorithms used for sampling the resulting posterior distribution.

2.3 Data

The largest SNIa compilation to date is the 'Pantheon sample' (Scolnic et al. 2018a), which contains 1048 spectroscopically confirmed SNIa. This compilation includes 279 new SNIa discovered by the Pan-STARRS1 (PS1) Medium Deep Survey (Chambers et al. 2016) in addition to the previous SNe discovered by previous catalogues to create the total.

   Unfortunately, the Pantheon sample only provides estimates (and associated uncertainties) of the distance modulus for each SNIa but does not include the covariance matrices of both the measurement error for each SNIa and the systematic covariance matrix across the whole data set. Because our Bayesian hierarchical model also requires these covariances over the light-curve fit parameters as opposed to the covariance over distance modulus provided by the Pantheon data, we instead use the smaller 'Joint Light-Curve Analysis' (JLA) compilation (Betoule et al. 2014). Very recently, a 'Pantheon+' data set has been presented in Brout et al. (2022), increasing the set of spectroscopically confirmed SNe to 1550 in the redshift span 0.001 to 2.26. The data products of this larger set have not yet been released, so unfortunately we cannot use these data in our framework. The JLA data contains 740 SNIa including 374 SNIa from the SDSS-II survey (Frieman et al. 2008; Sako et al. 2018), 239 from SNLS (Conley et al. 2011; Sullivan et al. 2011), a low-z sample of 118 SNIa at $z < 0.1$ which is comprised of numerous smaller surveys and nine *Hubble Space Telescope* SNIa. These have been fit and standardized using the SALT2 Light-Curve Fitter (Guy et al. 2007).

   An overview of the distribution of JLA objects in the sky is provided in Fig. 1. The long stripe in the lower left hemisphere is from the *SDSS* objects. It is clear to see that the distribution of the JLA objects in the sky is highly anisotropic.

2.4 Accounting for colour-dependent selection effects

Towards the high end of the redshift range of a given survey, SNe that are intrinsically brighter (smaller M_i) or bluer (smaller c_i) are more likely to be observed and to be followed up spectroscopically to confirm their type. This selection bias must be accounted for to avoid bias in the estimates of the cosmological parameters. Ignoring magnitude-based selection effects leads to estimates of the distance modulus that are biased low: at a given redshift, the average observed magnitude is smaller (i.e. the observed peak flux brighter) than the population mean, which leads to an estimated distance modulus that is biased low. This effect reduces or even obliterates the preference
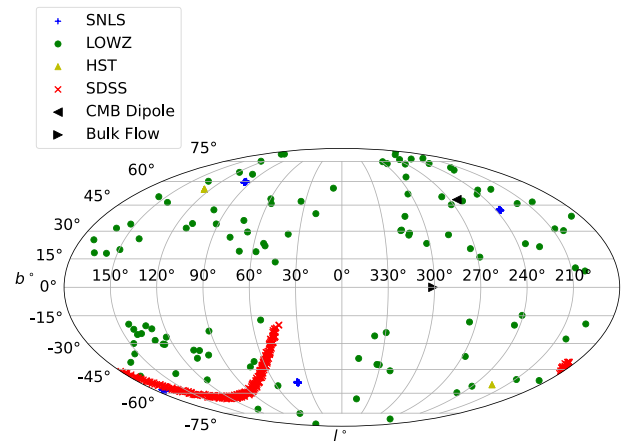

Figure 1. A plot of the JLA SNe showing their location in the sky in Galactic coordinates, as well as the direction of the CMB dipole (left-pointing triangle) and bulk flow (right-pointing triangle), as determined by Boruah et al. (2021).

for a non-zero cosmological constant. Traditionally, this has been addressed by 'correcting back' the estimates of the distance modulus by the average bias in each redshift bin, established with forward simulations of data subject to selection effects. This approach is adopted e.g. by Betoule et al. (2014). More recently, this method has been extended and refined with the so-called 'BEAMS with Bias Corrections' (BBC) method (Kessler & Scolnic 2017). The JLA analysis only corrected for magnitude-based selection effects, concluding that no additional correction were necessary for colour [Betoule et al. (2014), Fig. 11], despite observing a downward trend in observed colour with redshift for SNSL and *SDSS*.

   In the context of a Bayesian analysis, however, selection effects are treated differently: the posterior is conditional on the observed data (Kelly 2007), which leads to a re-weighing factor increasing the statistical weight of SNe that are less likely to be observed (see equation 23 below). Rubin et al. (2015) introduced a general formalism for the selection function that was further developed by Hinton et al. (2018). In practice, however, this formalism typically requires several simplifying assumptions that may be difficult to justify (e.g. a well-sampled SNIa redshift distribution, a selection function that is described by a normal cumulative distribution function (CDF), independence of the selection probability from the underlying cosmology). We will present an improved selection effects treatment in an upcoming, dedicated work.

   Rubin & Hayden (2016) argue that uncorrected-for colour-dependent selection effects remaining in the JLA data (after bias correction of the data) should be addressed by introducing a population colour mean that is both redshift- and survey-dependent. However, at the top level of the BHM we would like a *physically meaningful* population mean that describes the underlying, population-level latent mean colour, itself a reflection of the physical properties of the SNe. Such a colour mean can be a function of redshift, to reflect evolution in the physical properties of SNe with lookback time, but it cannot be survey-dependent, for clearly the latter dependency is caused by survey-specific selection effects and, in virtue of being survey-specific, *cannot* be the consequence of changing underlying physical properties of the SNe being observed. Thus, by using population-level variables to address a survey-induced selection effect, the method advocated by Rubin & Hayden (2016) goes against the physical interpretability of the BHM; we prefer the population-level variables to be tied to the physics of the SNIa explosion mechanism rather than the survey-induced selection

effects. Furthermore, as pointed out by Dam, Heinesen & Wiltshire (2017), modelling residual colour drift with redshift as advocated by Rubin & Hayden (2016) introduces undesirable degeneracies with cosmological parameters in the cosmographic expansion.

Here, we account for residual colour-based selection effects with an approximate method that captures the spirit of the correct Bayesian procedure. (We will present a more complete exposition in an upcoming work.) In general, we aim to base the likelihood function on the distribution of the data d_i for SNIa i conditional on it having been observed, which is denoted by an indicator variable $I_i = 1$. ($I_i = 0$ would indicate that SNIa i is not observed.) Denote by $\hat{D} = \{\hat{d}_1, \ldots, \hat{d}_n\}$ a random sample of SNe where all SNe have equal probability of being observed (i.e. there are no selection effects in $\hat{D}$). In the presence of selection effects, we observe a non-representative sample of $n_{\mathrm{obs}} < n$ SNe from $\hat{D}$, whereby a SNIa i is observed with probability given by the selection function $p(I_i = 1|\hat{d}_i, \Psi)$, where $\hat{d}_i$ are the observed (noisy) data, and Ψ are parameters describing the selection function (assumed known). The distribution of the observed $\hat{d}_i$, conditional on SNIa i being observed, is given by

$$p(\hat{d}_i|I_i = 1, \Psi, \Theta) = \frac{p(I_i = 1|\hat{d}_i, \Psi)p(\hat{d}_i|\Theta)}{p(I_i = 1|\Psi, \Theta)}, \qquad (21)$$

where $\Theta = \{\mathscr{P}_a, \vartheta\}$ are the parameters of the hierarchical model (including the parametrization of the distance modulus, $\mathscr{P}_a$, and the population-level distribution parameters, ϑ). We assume that the selection probability conditional on the observed data, $\hat{d}_i$, i.e. $p(I_i = 1|\hat{d}_i, \Psi)$ in the numerator of (21), does not depend on Θ and thus is an ignorable constant if (as we assume here) the selection function and its parameter Ψ are known. The quantity $p(\hat{d}_i|\Theta)$ is the likelihood in the absence of selection effects, and the denominator gives the probability of observing a SNIa, irrespective of the value of the data:

$$p(I_i = 1|\Psi, \Theta) = \int d\hat{d}_i\, p(I_i = 1|\hat{d}_i, \Psi)p(\hat{d}_i|\Theta). \qquad (22)$$

Omitting the ignorable multiplicative constants in the numerator of (21) yields the likelihood function of Θ including selection effects for a sample of n_{obs} observed SNe, $\hat{d}_{\mathrm{obs}} \equiv \{\hat{d}_1, \ldots, \hat{d}_{n_{\mathrm{obs}}}\}$,

$$p(\hat{d}_{\mathrm{obs}}|\{I_i = 1\}_{i=1}^{n_{\mathrm{obs}}}, \Psi, \Theta) \propto \frac{p(\hat{d}_{\mathrm{obs}}|\Theta)}{p(I = 1|\Psi, \Theta)_{\mathrm{obs}}^n}, \qquad (23)$$

where we have dropped the dummy index i in the denominator. Therefore, selection effects are accounted for by dividing the likelihood function of the observed data, $p(\hat{d}_{\mathrm{obs}}|\Theta)$, by a 'correction factor' that gives the probability of making n_{obs} observations.

Thus far, we have been entirely general. Next we specify the form of the selection function, $p(I_i = 1|\hat{d}_i, \Psi)$, entering in equation (22). The probability of a SNIa being selected, and spectroscopically followed-up to determine its type, depends primarily on its magnitude and colour. (SNe with larger stretch parameter x_1 are slower declining and thus remain visible and potentially detectable for longer, but this effect is subdominant.) The data correction procedure in Betoule et al. (2014) should in principle account for both magnitude- and colour-based selection, but their discussion makes it clear that there are large uncertainties in the determination of the selection probability that enters their forward simulation of the data. For example, Betoule et al. (2014) mention that the *SDSS* spectroscopic follow-up target selection favours intrinsically bluer SNe, introducing complex colour-dependency in the selection function. In light of such difficult-to-simulate selection effects, we advocate a method that estimates any residual selection effect [after the data correction procedure of Betoule et al. (2014)] directly from the observed data.

We wish to account for residual colour-based selection effects that may remain in the data. Therefore, we assume that $p(I_i = 1|\hat{d}_i, \Psi)$ depends only on $\hat{c}_i$ and $\hat{z}_{\mathrm{hel},i}$, with the N_s redshift bins for survey s chosen as discussed in Section 2.3, and factorize both the selection function and the likelihood in a product over redshift and survey bins, assumed independent of each other. Within each redshift, and survey bin, we allow a different selection function, which is derived below. With these assumptions, the probability of observing n_{obs} SNe is (with the shorthand notation $I_{n_{\mathrm{obs}}} = 1$ denoting $\{I_1 = 1, \ldots, I_{n_{\mathrm{obs}}} = 1\}$):

$$p(I_{n_{\mathrm{obs}}} = 1|\Psi, \Theta)$$
$$= \prod_{s=1}^{4} \prod_{j=1}^{N_s} \left(\int d\hat{d}_i\, p_{sj}(I_i = 1|\hat{d}_i, \Psi)p_{sj}(\hat{d}_i|\Theta) \right)^{N_{sj}}, \qquad (24)$$

where N_s is the number of bins for survey s and N_{sj} the number of observed SNe in bin sj. Within each redshift bin for survey s, we parametrize the selection function as a normal cumulative distribution function (CDF), and assume that we observe a SNIa i with colour $\hat{c}_i$ with probability:

$$p_{sj}(I_i = 1|\hat{d}_i, \Psi) = \Phi\left(\frac{c_{sj}^{\mathrm{obs}} - \hat{c}_i}{\sigma_{sj}^{\mathrm{obs}}}\right), \qquad (25)$$

where

$$\Phi(x) = \int_{-\infty}^{x} \mathcal{N}_y(0, 1)\mathrm{d}y \qquad (26)$$

is the CDF of a standard normal, and $\mathcal{N}_y(\mu, \sigma^2)$ is a Gaussian distribution in y with mean μ and variance σ^2. In equation (25), c_{sj}^{obs} is the colour value at which there is a 50 per cent probability of observing a SNIa *in redshift bin j and for survey s*; $\sigma_{sj}^{\mathrm{obs}}$ denotes the width of the transition from the regime where all objects are observed, i.e. for $(c_{sj}^{\mathrm{obs}} - \hat{c}_i)/\sigma_{sj}^{\mathrm{obs}} \ll 0$, to the regime where no objects are observed, where $(c_{sj}^{\mathrm{obs}} - \hat{c}_i)/\sigma_{sj}^{\mathrm{obs}} \gg 0$, for the bin sj being considered. In equations (31)–(32) below we show how to estimate the selection function parameters $\Psi = \{(c_{sj}^{\mathrm{obs}}, \sigma_{sj}^{\mathrm{obs}})\}$ ($s = 1, \ldots, 4$, $j = 1, \ldots, N_s$). As an approximation, we ignore uncertainty in the resulting estimates and assume the parameters are known exactly.[3]

In principle, we would like to use the likelihood function of March et al. (2011) and Shariff et al. (2016) as the second term of the integrand in equation (22). Since we only wish to account for residual colour-based selection effects, however, we ignore the part of the BAHAMAS likelihood that relates colour to magnitude via the Tripp linear relation [equation (C2) in March et al. (2011)], and instead only consider the distribution of colour values that one would obtain when integrating out the latent colour variables conditional on all other variables in the BHM, leading to the simple expression for the likelihood entering into equation (24):

$$p_{sj}(\hat{d}_i|\Theta) = \mathcal{N}_{\hat{c}_i}\left(c_\star, R_c^2 + \bar{\sigma}_{c,sj}^2\right), \qquad (27)$$

where $\bar{\sigma}_{c,sj}$ is the average colour measurement error for the n_{sj} SNe in bin sj (for simplicity, we assume all n_{sj} SNe in bin sj have the same colour measurement error, given by $\bar{\sigma}_c$; we also ignore correlation between colour and stretch and magnitude).

Equation (27) features a redshift-independent conditional expectation of colour, described by $c_\star$. This formalizes the assumption of Rubin & Hayden (2016) within BAHAMAS that the observed drift to bluer SNe with redshift within a survey is a consequence of selection

---

[3]We ignore uncertainty in our estimates of Ψ, and we defer the evaluation of the impact of this approximation to an upcoming, dedicated work.

effects and not of a change in the underlying population colour distribution with redshift.

With the above elements, we can compute the probability of observing SNIa i in redshift bin j for survey s by integrating over its colour, $\hat{c}_i$, obtaining[4]

$$p_{sj}(I_i = 1|\Psi, \Theta) = \Phi\left(\frac{c_{sj}^{\mathrm{obs}} - c_\star}{\sqrt{\left(\sigma_{sj}^{\mathrm{obs}}\right)^2 + R_c^2 + \bar{\sigma}_{c,sj}^2}}\right). \quad (28)$$

For a given sj bin, when $c_\star \ll c_{sj}^{\mathrm{obs}}$ selection effects are irrelevant, because the survey is seeing the entire colour population, and accordingly $p(I_i = 1|\Psi, \Theta) \to 1$ from equation (28). However, $p(I_i = 1|\Psi, \Theta)$ becomes smaller for values of $c_\star > c_{sj}^{\mathrm{obs}}$, with the difference measured in units of the total standard deviation, i.e. when the survey is preferentially seeing the bluer part of the population because of colour-based selection bias. In this case, the observed distribution of the N_{sj} objects in the sj bin deviates from the latent distribution, and the likelihood that ignores selection effects would incorrectly penalize this value of $c_\star$. According to equation (23), the correction factor in the denominator of equation (23) increases the weight given to observed SNe with $c_\star > c_{sj}^{\mathrm{obs}}$.

Finally, there remains the issue of determining the value of Ψ, the selection function parameters. Ideally, one would do so from forward simulation of surveys, but this is unpractical for our purposes, and unfeasible for the low-z sample, which is obtained from a collection of telescopes with poorly understood selection functions. Furthermore, as noted earlier, colour-based selection effects might escape *ab initio* modelling of this kind, as indicated in e.g. Betoule et al. (2014). As an alternative, we estimate the value of Ψ in each redshift- and survey-bin sj, by matching the first and second moment of the empirical colour distribution within the bin to the marginal distribution of colour based on the right-hand side of (23), understood as a distribution over observed colour values $\hat{c}_i$ within each bin. Let $m_C(t)$ denote the moment generating function of the random variable C (the observed colour), defined as

$$m_C(t) \equiv \int_{-\infty}^{\infty} e^{ty} f_C(y)\,dy, \quad (29)$$

where $f_C(c)$ in our case is given by (in the bin under consideration)

$$f_C(c) = \frac{\mathcal{N}_c\left(c_\star, R_c^2 + \bar{\sigma}_{c,sj}^2\right)\Phi\left(\frac{c_{sj}^{\mathrm{obs}} - c}{\sigma_{sj}^{\mathrm{obs}}}\right)}{p_{sj}(I_i = 1|\Psi, \Theta)}, \quad (30)$$

with denominator given by equation (28). Our strategy, known as the *method of moments*, is to analytically compute the first two moments of the distribution, set them equal to the empirical moments, and solve the resulting system of equations to obtain estimates of the selection function parameters in each survey and redshift bin, $\{c_{sj}^{\mathrm{obs}}, \sigma_{sj}^{\mathrm{obs}}\}$. Details of the calculation are presented in Appendix A, where we show that the moment generating function is given by equation (A5), its first moment, $dM_C(t)/dt|_{t=0}$, by equation (A18), and its second moment, $d^2M_C(t)/dt^2|_{t=0}$, by equation (A19). Specifically, in each bin, we set the first moment equal to the empirical mean, and set the second central moment equal to the empirical variance:

$$\left.\frac{dM_C(t)}{dt}\right|_{t=0} = \langle \hat{c}_i \rangle, \quad (31)$$

[4]It is useful to recall that $\int_{-\infty}^{\infty} \Phi\left(\frac{\mu-x}{\sigma}\right)\mathcal{N}_x(\nu, \tau^2)dx = \Phi\left(\frac{\mu-\nu}{\sqrt{\sigma^2+\tau^2}}\right)$.

$$\left.\frac{d^2M_C(t)}{dt^2}\right|_{t=0} - \left.\frac{dM_C(t)}{dt}\right|_{t=0}^2 = \frac{1}{1-N_{sj}}\sum_{i=1}^{N_{sj}}(\hat{c}_i - \langle \hat{c}_i \rangle)^2, \quad (32)$$

where $\langle \hat{c}_i \rangle = \frac{1}{N_{sj}}\sum_{i=1}^{N_{sj}}\hat{c}_i$ is the empirical mean. We set the population mean and standard deviation to $c_\star = -0.0022$ and $R_c = 0.0758$, the empirical mean and standard deviation from the lowest two bins of the *SDSS*, SNLS, and low-z surveys, where colour-based selection effects are expected to be negligible. We then solve the resulting coupled equations to determine $\{c_{sj}^{\mathrm{obs}}, \sigma_{sj}^{\mathrm{obs}}\}$.

In cases where N_{sj} is small (~ 10) and the sample variance is small, the method of moments yields an estimate of $\sigma_{sj}^{\mathrm{obs}}$ near or equal to zero. This is similar to a well-known pathology in the estimation of the shape parameter in the skew-normal distribution (see e.g. Azzalini & Arellano-Valle 2012). A simple solution is to impose a lower cutoff to the value of $\sigma_{sj}^{\mathrm{obs}}$. We chose a cutoff value $\sigma_{sj}^{\mathrm{obs}} > 0.01$, since any smaller value leads to a selection function indistinguishable from a step function. Tests of our method of moments on simulated data are provided in Appendix A.

Because our selection effect model assumes in equation (27) that the colour observations are independent, we set the corresponding covariances in the variance-covariance matrix for the systematic effects to zero. This has a minor effect on our estimates of the cosmological parameters, as those terms are subdominant with respect to other off-diagonal terms.

We apply the method of moments to estimate Ψ to each the four sub-surveys separately, and we verify its accuracy by simulating colour observations from the model of equation (27), assuming a Normal constant-in-redshift latent colour distribution with mean $c_\star = 0$ and standard deviation $R_c = 0.1$. We then apply the reconstructed selection function in each redshift bin, and compare the resulting distribution of simulated SNe with the observed sample within that bin. This comparison is shown in Fig. 2. For the simulation study and the real JLA data in Section 3.2, we divided each sub-survey in 5 approximately equal-spaced redshift bins, with the following exceptions: the *HST* data is treated in one single bin owing to the small number of SNIa in *HST*. For the same reason, in the low-z survey data, the two highest redshift bins are combined into a single bin. For the *SDSS* survey, the right edge of the 4th bin has its boundary shifted 0.015 in redshift space to the right, in order to account for a discontinuity in the data, where the population of objects have a lower colour and are separated by a gap in redshift. The agreement between real data and simulation is excellent, thus validating our approach.

2.5 A new derivation of peculiar velocity corrections

Our motion w.r.t. the CMB frame is measured precisely by the temperature dipole observed in CMB anisotropies. The most accurate result is from Planck Collaboration I (2020), giving a velocity $v_{\odot-\mathrm{CMB}} = 369.82 \pm 0.11$ km s^{-1} in the direction $l = 264.021°\pm 0.011°$, $b = 48.253° \pm 0.005°$. This induces in the non-relativistic limit a redshift correction (Davis et al. 2011)

$$z_{\mathrm{pec}}^{\odot} \approx -\frac{v_{\odot-\mathrm{CMB}}}{c}(\mathbf{n}_{\mathrm{CMB}} \cdot \mathbf{n}_{\mathrm{SN}}) \lesssim 10^{-3}, \quad (33)$$

where $\mathbf{n}_{\mathrm{CMB}}$ is a unit vector in the direction of the CMB dipole and $\mathbf{n}_{\mathrm{SN}}$ is a unit vector in the direction of the SNIa. Given the small uncertainties in the measurement for $v_{\odot-\mathrm{CMB}}$ and the CMB dipole direction, we can consider $z_{\mathrm{pec}}^{\odot}$ as known exactly, and thus neglect measurement error on this quantity (as it is $\sim 3 \times 10^{-7}$). Estimating $z_{\mathrm{pec}}^{\mathrm{SN}} = v_{\mathrm{pec}}^{\mathrm{SN}}/c$ requires knowledge of the peculiar velocity of the SNIa
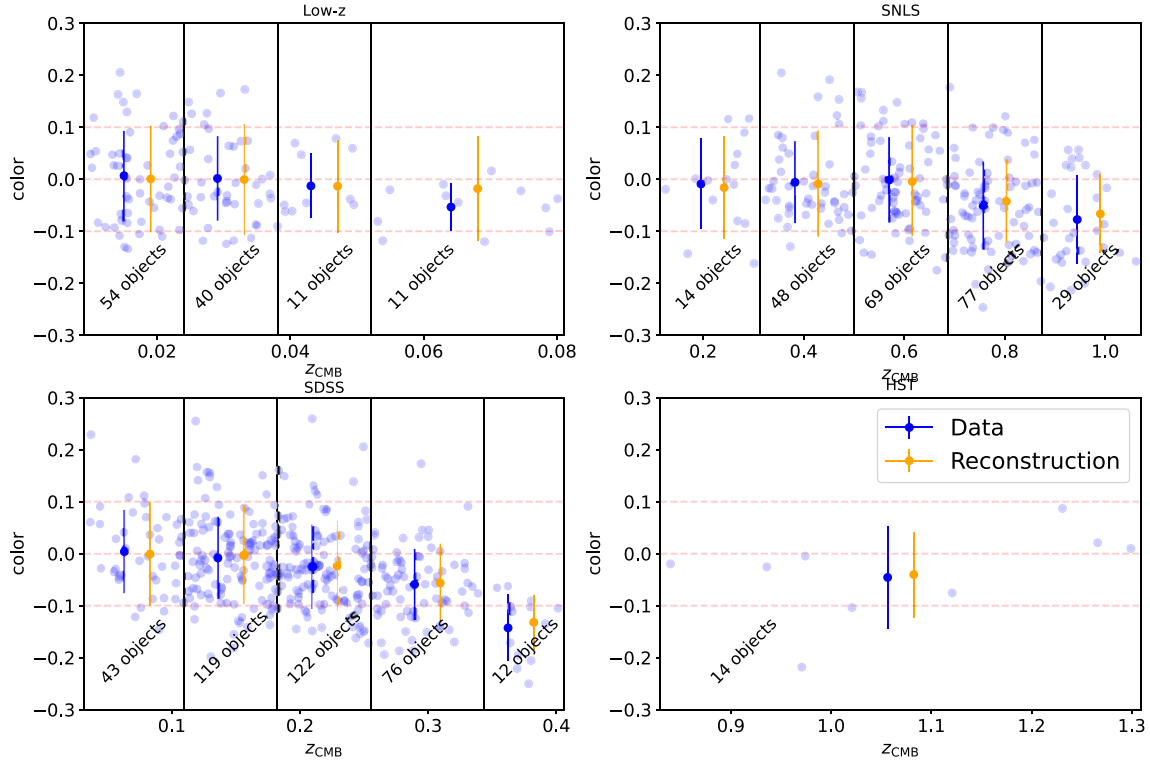
Figure 2. Colour-based selection function in binned JLA data, with redshift bins boundaries indicated by the vertical black lines. The blue circles are the individual SNe, the blue errorbars represent the data mean and standard deviation within each top-hat bin, while the orange errorbars give the mean and standard deviation of simulated data from the model using the reconstructed selection function in that bin (shifted horizontally for ease of comparison).

in the CMB frame, v_{pec}^{SN}. This can be measured either from a peculiar velocity field survey [for example, by using the Fundamental Plane (FP) relation or the Tully–Fisher (TF) relation to measure the distance to a galaxy, and then subtracting from the observed velocity the expansion component obtained from the Hubble–Lemaître law) or derived from linear perturbation theory applied to a smoothed density field. The latter approach has a long history, originally having been used to predict the peculiar velocities of FP and TF samples (Hudson 1993; Strauss & Willick 1995; Davis, Nusser & Willick 1996) but more recently applied to peculiar velocity data that include SNe type Ia. (Riess et al. 1997; Radburn-Smith, Lucey & Hudson 2004; Pike & Hudson 2005; Neill, Hudson & Conley 2007; Turnbull et al. 2012; Carrick et al. 2015; Boruah et al. 2020; Lilow & Nusser 2021; Stahl et al. 2021).

While the peculiar velocity of the SNIa becomes rapidly negligible for $z \gtrsim 0.1$, it is important for local objects ($z \ll 0.1$), where it can be significant w.r.t. the expansion velocity (up to ~30 per cent) and where it leads to much larger changes in the apparent magnitude, due to the steeper gradient of the distance modulus at low redshift. For example, at $z = 0.01$ an uncorrected SNIa peculiar velocity v_{pec}^{SN} induces a redshift systematic error $\delta z = v_{pec}^{SN}/c$, which corresponds to a significant change in the theoretical distance modulus $\delta\mu \approx \frac{d\mu}{dz}\delta z \approx 5/\ln(10)(\delta v/(cz)) = 0.14$ mag for $v_{pec}^{SN} = 200$ km s^{-1}. To avoid difficulties with peculiar velocities, earlier SNIa cosmological analyses routinely adopted a lower redshift cutoff z_{cut}, removing SNe below z_{cut}; for example, Kessler et al. (2009) used $z_{cut} = 0.02$; Riess et al. (2007) used $z_{cut} = 0.023$. Recently, Huterer (2020) estimated the impact of uncorrected peculiar velocities on the Pantheon sample from numerical N-body simulations, and recommended a cutoff $z_{cut} = 0.02$ to protect against significant bias to cosmological parameters.

However, a better way that does not discard useful data at low redshift is to assign uncertainties that scale with distance, as we do here.

The JLA sample contains 37 SNe with $z_{hel} < 0.02$, and 110 with $z_{hel} < 0.05$, for which an appropriate treatment of peculiar velocities is required if they are to be used in the cosmological analysis – particularly in our case, where we wish to use them to constrain a local dipole in the expansion. To first order in redshift equation (2) gives

$$\bar{z} = z_{hel} - z_{pec}^{\odot} - z_{pec}^{SN}, \tag{34}$$

meaning that the redshift of a comoving observer, $\bar{z}$, is obtained from the measured heliocentric redshift by subtracting our local dipole ($z_{pec}^{\odot}$) and the redshift due to the SNIa peculiar velocity, z_{pec}^{SN}.

The model used in Betoule et al. (2014) to estimate z_{pec}^{SN} has been criticized by C19, who highlighted potential bulk flow velocity discontinuities at $z = 0.04$, pointed out that peculiar velocity corrections arbitrarily disappear beyond 200 h^{-1} Mpc ($z \sim 0.067$, the limit of the galaxy density field measurements from which the peculiar velocities were derived) and that the residual uncorrelated velocity dispersion of $\sigma_v = 150$ km s^{-1} might be underestimated. While RH20 pointed out technical flaws with the analysis of C19, it is important in the light of this valid criticism to revisit the issue of low-redshift peculiar velocity corrections here.

To this end, in this work we replace the peculiar velocity corrections used by Betoule et al. (2014) – which rested on the IRAS PSCz catalogue from Branchini et al. (1999) – with the more recent ones obtained by Carrick et al. (2015). We follow Boruah et al. (2020, 2021), who carried out a thorough comparison between density reconstruction from galaxy redshift surveys and kernel smoothing of peculiar velocity data methods. We adopt here their peculiar velocity

field inferred from 69 160 galaxies from the 2M++ galaxy redshift catalogue (Lavaux & Hudson 2011). The catalogue covers almost the entire sky (with the notable exception of the plane of our galaxy), is highly complete out to $200\,h^{-1}$ Mpc ($z \sim 0.067$) in the region covered by 6dF and *SDSS*, and out to $125\,h^{-1}$ Mpc ($z \sim 0.041$) in the region covered by 2MRS. We thus remove[5] the SNIa peculiar velocity corrections for the low-z JLA sample that are in common with the A2 sample of Boruah et al. (2021) (107 objects), and replace them with new values obtained as follows.

The radial peculiar velocity for a SNIa at comoving distance r and direction $\mathbf{n}_{SN}$ is obtained from the luminosity-weighted density field $\mathbf{v}_{gal}$ as

$$v_{pec}^{SN}(r, \mathbf{n}_{SN}, \theta) = \mathbf{n}_{SN} \cdot (\beta_v \mathbf{v}_{gal}(r, \mathbf{n}_{SN}) + \mathbf{V}_{ext}), \qquad (35)$$

where $\theta = \{\beta_v, \mathbf{V}_{ext}\}$, with a rescaling parameter $\beta_v = 0.411 \pm 0.020$ and external residual bulk flow velocity (in Galactic Cartesian coordinates) $\mathbf{V}_{ext} = [52 \pm 20, -163 \pm 21, 49 \pm 16]$ km s^{-1} (how we treat and propagate the uncertainties in these values is addressed in Section 2.6). We follow the methodology of Boruah et al. (2021), with the difference that we only use the SFI++ peculiar velocity sample (therefore not including A2 SNe data) in order to avoid circularity (i.e. using SNe data to predict the peculiar velocity correction for the same SNe data).

We do not wish to use the distance modulus information from a SNIa at this stage of the analysis, only its observed redshift in the CMB rest frame, $\hat{z}_{CMB} \equiv \hat{z}_{hel} - z_{pec}^{\odot}$. First, the observed redshift in the CMB rest frame is corrected to the average redshift of the group to which the host galaxy belongs. Differently from JLA, we correct the CMB rest frame redshift for *all* host galaxies, including those in clusters and poorer groups. This is necessary to suppress the highly non-linear velocity contribution to the observed redshift, and it leads to deviations of a few percent in $\hat{z}_{CMB}$ in most low-z SNe, compared with the value used by JLA, see Fig. 3. However, there are 6 SNe that show much larger changes in their CMB frame redshift, up to $\sim$30 per cent (highlighted in green in Fig. 3); two of them (**sn2007ci** and **sn2001cz**) are in common with the outliers in peculiar velocity, identified in Fig. 4. It is worth noting that Carr et al. (2021) reviewed Type Ia SNe literature and discovered that some SNIa had been reported with incorrect redshifts and/or positions due to misprints. Two of the outliers in Fig. 4, **sn2008bf** and **sn1996c**, are among the SNIa identified by Carr et al. (2021) as requiring updates: **sn2008bf** suffers from an uncertain host galaxy identification, while **sn1996c** had an incorrect sky location. Many other SNIa had their redshifts and positions updated by Carr et al. (2021), but their data set is not publicly available yet and therefore we cannot make use of their findings.

We compute the expected peculiar velocity by marginalizing over the unknown comoving distance of the SNIa, r:

$$\langle v_{pec}^{SN} \rangle = \int dr\, p(r|c\hat{z}_{CMB}) v_{pec}^{SN}(r, \mathbf{n}_{SN}), \qquad (36)$$

where v_{pec}^{SN} is computed self-consistently from the flow model, equation (35), and $p(r|\hat{z}_{CMB})$ is the probability density function (pdf) for r given the observed redshift. This can be linked via a variable transformation to the pdf for the true (latent) CMB redshift of the

SNIa, $z_{CMB}(r)$, via:

$$p(r|c\hat{z}_{CMB}) = p(cz_{CMB}(r)|c\hat{z}_{CMB}) \left| \frac{\partial cz_{CMB}(r)}{\partial r} \right|, \qquad (37)$$

where from equation (3)

$$z_{CMB}(r) = \bar{z}(r) + (1 + \bar{z}(r))v_{pec}^{SN}(r, \mathbf{n}_{SN})/c, \qquad (38)$$

and the cosmological redshift at comoving distance r, $\bar{z}(r)$, is computed for the ΛCDM concordance model, with parameters as in Table 1. Note that the transformation between r and z_{CMB} may not be unique due to the existence of triple-valued regions. However, in practice we checked that the reconstructed velocity field indeed leads to unique transformation between r and z_{CMB} for the parameters under consideration. Nevertheless, it can lead to 'flat' regions in redshift space (i.e., where $\frac{\partial z_{CMB}}{\partial r} \approx 0$), which result in large uncertainties in the expected peculiar velocity.

The 2M++ reconstruction employs linear perturbation theory to predict the velocities. As shown in Carrick et al. (2015), this leads to an uncertainty due to non-linearities of $\sigma_v^{NL} = 150$ km s^{-1}. Therefore, assuming a Gaussian uncertainty, we can write the probability of the predicted redshift in the CMB frame for a SNIa at comoving distance r given its observed redshift transformed in the CMB frame in equation (37) as

$$p(cz_{CMB}(r)|c\hat{z}_{CMB}) = \mathcal{N}\left(c\hat{z}_{CMB}, \left(\sigma_v^{NL}\right)^2\right). \qquad (39)$$

As a check for the robustness of our method, we also estimated the predicted peculiar velocity using an iterative prescription. In this alternative method, we start from the observed CMB rest frame redshift as an initial, rough approximation for the comoving distance (under the fiducial ΛCDM assumption), taking $v_{pec}^{SN} = 0$. In subsequent iterations, an updated estimate for the comoving distance is obtained using equation (38) and the velocity estimate we get from the reconstruction at the given comoving distance. This step is repeated until convergence. The iterative method gives broadly consistent results as the marginalization-based method described above. However, the iterative prescription may underestimate the uncertainty in the vicinity of triple-valued regions, and therefore we elected to use the marginalization method instead.

Our new peculiar velocity corrections obtained from equation (36) are compared against those used in Betoule et al. (2014) in Fig. 4, which are obtained from the JLA data products via[6]

$$v_{corr, JLA} = c \left(\frac{1 + z_{hel}}{(1 + \bar{z})(1 + z_{pec}^{\odot})} - 1 \right). \qquad (40)$$

The correlation coefficient between our peculiar velocity corrections and that used in Betoule et al. (2014) is only $\sim$0.60. There are also 6 SNe (labelled in Fig. 4) that are more than 3 standard deviations of the sample away from the identity line. Several reasons can explain the differences between our peculiar velocities and those used in JLA: first, the density field used to predict peculiar velocities in JLA was based on the IRAS PSCz survey, which is likely to be noisier than 2M++ everywhere. Secondly, in the JLA analysis only galaxies in rich clusters are corrected to the mean redshift of the cluster, whereas here we correct the CMB rest frame redshift for all host galaxies, including those in clusters and poorer groups.

For SNe beyond $z = 0.067$ (in the SNLS, *SDSS* and high-z samples), the relative importance of the peculiar velocity corrections

---

[5]Differently from C19, we do not remove the magnitude bias corrections made to the JLA SNe, as they are important to account for selection effects, nor do we neglect the contribution of peculiar velocities uncertainty to the covariance matrix, which we re-derive for our case.

[6]In equation (40) we use the notation introduced in this paper but we notice that our $\bar{z}$ is (confusingly) denoted 'z_{CMB}' in the Betoule et al. (2014) and associated data products.
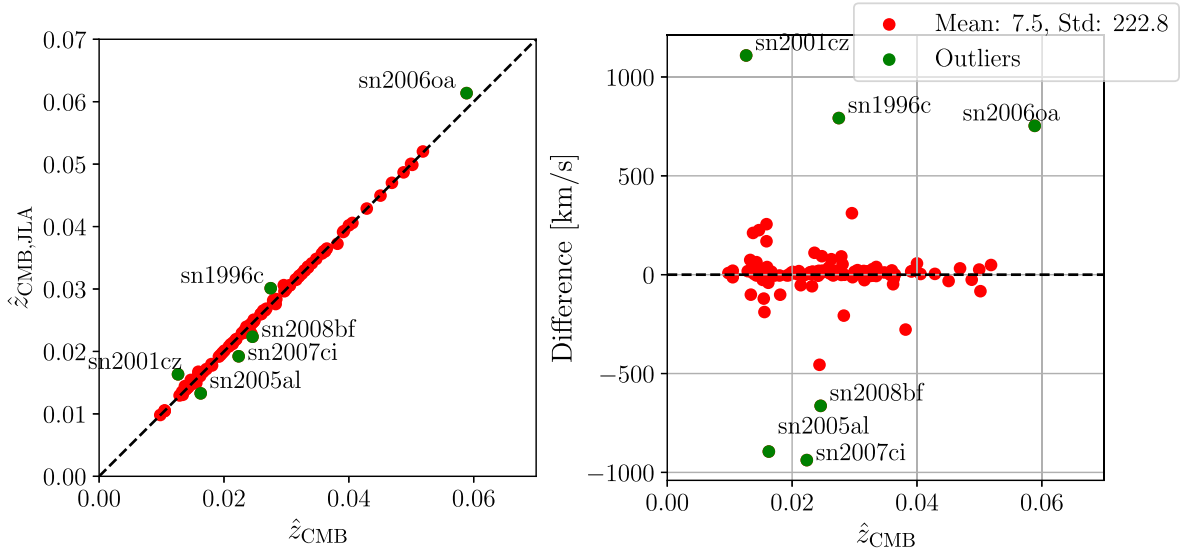
Figure 3. Left-hand panel: comparison of the CMB rest-frame redshift used in this work for the low-redshift sample (horizontal axis, 107 SNe) with that of the JLA analysis (vertical axis). There are 6 SNe (highlighted in green) with a difference exceeding 3 standard deviations around the identity line (dashed). Right-hand panel: the same comparison but showing the fractional differences between redshifts on the vertical axis.
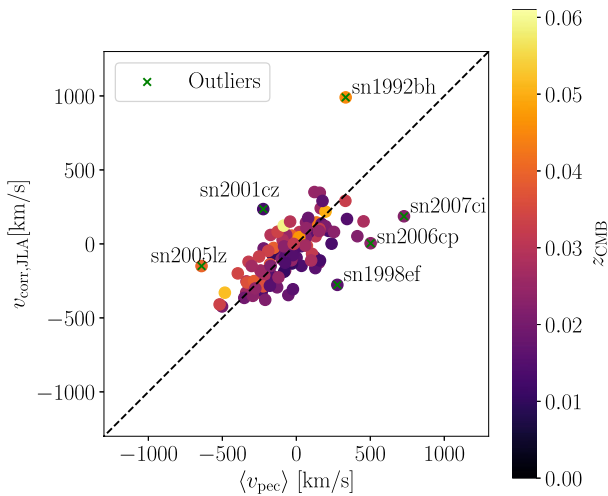

Figure 4. Comparison of the peculiar velocity corrections used in this work (horizontal axis) with those adopted in the JLA analysis (vertical axis) for the 107 SNe in the A2 low-redshift sample common to the JLA data. The colour coding gives the CMB rest-frame redshift used in this work. Outliers (defined as more than 3 standard deviations away from the dashed identity line) are labelled.

diminishes as the recession velocity of the Hubble flow increases, so the detailed treatment becomes less important. In the JLA analysis, peculiar corrections have been set to 0 beyond redshift $z \sim 0.067$, the limit of the galaxy survey from which said corrections were derived. We do the same here, noting that beyond redshift $z \sim 0.067$ the exact treatment of peculiar velocity correction becomes less crucial since their relative importance diminished quickly.

2.6 Peculiar velocity correction uncertainties

As we have replaced the peculiar velocities of JLA with our own, new estimates, we also update their error analysis associated with the peculiar velocities treatment. First, we remove the diagonal

term from the JLA statistical covariance matrix representing the uncertainty from peculiar velocity corrections. We also remove the 'pecvel' contribution to the systematic covariance matrix. We replace them with the following terms, flowing from our updated treatment of peculiar velocity corrections.

From equation (34), the covariance of the cosmological redshift value for SNe i, j is given by (without including the negligible error in $z_{\text{pec}}^{\odot}$) is given by

$$\Xi_{z,ij}^2 = \delta_{ij}^{\text{K}} \sigma_{z,i}^2 + \Sigma_{z,ij}^2, \tag{41}$$

$$\Sigma_{z,ij}^2 = \delta_{ij}^{\text{K}} \left(\sigma_{\text{NL}}^2 + \sigma_{\text{2M++}}^2(z_{\text{CMB}}) + \sigma_{v,i}^2 \right) / c^2 + C_{ij}^{\text{flow}} / c^2, \tag{42}$$

where $\sigma_{z,i}$ is the spectroscopic redshift measurement uncertainty, $\sigma_{\text{NL}} = 150 \text{ km s}^{-1}$ is the uncertainty in the peculiar velocity due to non-linearities, $\sigma_{\text{2M++}}$ is the redshift-dependent uncertainty due to survey incompleteness, $\sigma_{v,i}$ is the standard deviation of the average peculiar velocity prediction, equation (36), and C_{ij}^{flow} is the correlated covariance coming from uncertainty in the flow model (δ_{ij}^{K} is the Kronecker delta). We address each term in turn.

For the 107 low-z SNe in our analysis, the largest reported statistical uncertainty in their redshift measurement in the JLA data release is $\max_i \sigma_{z,i}^{\text{JLA}} = 0.0014$, corresponding to a velocity uncertainty of 420 km s^{-1}. The JLA data release also has $\sigma_{z,i}^{\text{JLA}} = 0$ for 10 of the 107 low-z SNe and $\sigma_{z,i}^{\text{JLA}} < 0$ for 42 SNIa. In order to resolve the issue of 0 or negative redshift uncertainties and to be conservative, we adopt the following prescription for the standard deviation of the spectroscopic uncertainty:

$$\sigma_{z,i} = \max \left(\sigma_{z,i}^{\text{JLA}}, 5 \times 10^{-4} \right), \tag{43}$$

where the floor value of 5×10^{-4} represents the typical uncertainty of spectroscopic redshift determination from host galaxies spectra.

The term $\sigma_{\text{NL}}^2 = 150 \text{ km s}^{-1}$ represents uncertainty in the linear velocity prediction due to unaccounted-for non-linearities, which we fix at the value recommended in Carrick et al. (2015). However, the uncertainty in our reconstructed peculiar velocity increases with redshift, an effect that was ignored in previous work: first, the predicted peculiar velocities for tracers near the outer edge of the

Table 1. Supernova population parameters, cosmological parameters, and dipole model parameters adopted in this work, together with the prior choices and fiducial values for simulation studies. 'SD' stands for standard deviation.

SNIa population distributions and covariates	Symbol	Fiducial value	Prior distribution
Mean absolute magnitude of SNIa	M_0	-19.3	$M_0 \sim \text{Normal}\,(-19.3, 2^2)$
Residual scatter of SNIa magnitude after corrections	σ_{res}	0.1	$\sigma_{\text{res}} \sim \text{InvGamma}\,(0.003, 0.003)$
Coefficient of stretch covariate	α	0.14	$\alpha \sim \text{Uniform}\,(0, 1)$
Coefficient of colour covariate	β	3.2	$\beta \sim \text{Uniform}\,(0, 4)$
Mean of stretch	x_*	0.0	$x^* \sim \text{Normal}\,(0, 10^2)$
Mean of colour	c_*	0.0	$c^* \sim \text{Normal}\,(0, 1^2)$
SD of stretch distribution	R_x	1.0	$R_x \sim \text{LogUniform}\,(-5, 2)$
SD of colour distribution	R_c	0.1	$R_c \sim \text{LogUniform}\,(-5, 2)$
Parameters controlling the expansion history			
Matter energy density	Ω_M	0.3	$\Omega_M \sim \text{Uniform}\,(0, 2)$
Dark energy density	Ω_Λ	0.7	$\Omega_\Lambda \sim \text{Uniform}\,(0, 2)$
Deceleration Parameter	q_0	-0.55	$q_0 \sim \text{Uniform}\,(-2, 1)$
Jerk and spatial curvature	$j_0 - \Omega_K$	1	$j_0 - \Omega_K \sim \text{Uniform}\,(-2, 2)$
Hubble–Lemaître constant (km^{-1} s^{-1} Mpc^{-1})	H_0	72	Fixed
Anisotropic expansion parameters			
Galactic longitude of dipole (rad)	l_d	$\{-, 4.60\}$	$l_d \sim \text{Uniform}\,(0, 2\pi)$
Galactic latitude of dipole (rad)	b_d	$\{-, 0.84\}$	$\cos(b_d) \sim \text{Uniform}\,(0, 1), b_d \in [0, \pi/2]$
Amplitude of dipole on μ	D_μ	$\{0, 0.02\}$	$D_\mu \sim \text{Uniform}\,(-0.2, 0.2)$
Amplitude of dipole on q_0	D_{q_0}	$\{0, 10\}$	$D_{q_0} \sim \text{Uniform}\,(-30, 30)$
Exponential scale of dipole	S	$\{-, 0.026\}$	$S \sim \text{Uniform}\,(0.01, 0.10)$

2M++ catalogue (200 Mpc h^{-1}) have larger uncertainty because of unaccounted-for structures outside of the survey limits, as well as because of lack of coverage beyond 125 Mpc h^{-1} for part of the sky (Hollinger & Hudson 2021); secondly, the noise increases at larger distances due to the smaller number of galaxies with larger weights that are used to represent the density field (Lilow & Nusser 2021). We capture these effects via the redshift-dependent term:

$$\sigma_{2\text{M}++}(z_{\text{CMB}}) = \begin{cases} \sigma_1 z_{\text{CMB}} & \text{for } z_{\text{CMB}} < z_{400}, \\ \sigma_1 z_{400} & \text{for } z_{\text{CMB}} \geq z_{400}, \end{cases} \quad (44)$$

where $z_{400} = 0.138$ is the redshift corresponding to a radial comoving distance of $400\, h^{-1}$ Mpc, and σ_1 is chosen so that the total peculiar velocity rms beyond z_{400}, i.e. $(\sigma_{\text{NL}}^2 + \sigma_{2\text{M}++}^2(z_{400}))^{1/2}$, equals 380 km s^{-1}. This prescription also approximately matches the ΛCDM prediction at the 2M++ boundary, $z = 0.067$, where $(\sigma_{\text{NL}}^2 + \sigma_{2\text{M}++}^2(0.067))^{1/2} = 227$ (km s^{-1}). This is in contrast with the original JLA analysis which uses a redshift-independent 150 km s^{-1} uncertainty throughout the redshift range.

The term $\sigma_{v,i}^2$ is the variance of $v_{\text{pec}}^{\text{SN}}$ under the distribution given by equation (37), i.e.

$$\sigma_{v,i}^2 = \left\langle \left(v_{\text{pec}}^{\text{SN}}\right)^2 \right\rangle - \left\langle v_{\text{pec}}^{\text{SN}} \right\rangle^2. \quad (45)$$

Finally, we translate the redshift covariance of equation (41) into a magnitude covariance via linear propagation of errors using the isotropic distance modulus of equation (11), i.e.

$$\sigma_{m,ij}^2 = \Sigma_{z,ij}^2 \left. \frac{\partial \mu_I}{\partial \bar{z}} \right|_{\substack{z_{\text{hel}} = \hat{z}_{\text{hel},i} \\ \bar{z} = \bar{z}_i}} \left. \frac{\partial \mu_I}{\partial \bar{z}} \right|_{\substack{z_{\text{hel}} = \hat{z}_{\text{hel},j} \\ \bar{z} = \bar{z}_j}}$$
$$+ \delta_{ij}^{\text{K}} \sigma_{z,i}^2 \left(\left. \frac{\partial \mu_I}{\partial z_{\text{hel}}} \right|_{\substack{z_{\text{hel}} = \hat{z}_{\text{hel},i} \\ \bar{z} = \bar{z}_i}} \right)^2 \quad (46)$$

where $\bar{z}_i$ is computed from equation (34), and the distance modulus derivatives are evaluated at the fiducial cosmological parameter values given in Table 1.

So far, we have considered a fixed value for the flow parameters, $\theta = \{\beta_v, \mathbf{V}_{\text{ext}}\}$ entering in equation (35). The uncertainties in the inferred flow parameters lead to correlated uncertainties in the peculiar velocities which needs to be accounted for, and that in previous work are usually considered a source of systematic error. Our parametrized flow model allows us to translate them into a statistical error, as follows. In order to estimate the covariance coming from uncertainty in the flow model parameters, we draw 10^4 posterior samples of the flow parameters θ_k ($k = 1, \ldots, 10^4$) from the fitted flow model, using the method of Boruah et al. (2020), and we calculate the average peculiar velocity, $\langle v_{\text{pec},i}^{\text{SN}} \rangle$ for all the 107 SNe in our low-z sample from those samples. We then estimate the covariance of the average peculiar velocity between SNIa i and j as $C_{ij}^{\text{flow}} = \text{Cov}(\langle v_{\text{pec},i}^{\text{SN}} \rangle, \langle v_{\text{pec},j}^{\text{SN}} \rangle)$, where the covariance matrix is computed from the k samples. Since the value of $\sigma_{v,i}$ above varies among the k samples (although the variation is small, $\gtrsim 10$ per cent), we use the average of $\sigma_{v,i}$ from the 10^4 posterior samples. In accord with terminology used in the literature, we call this term the 'systematic uncertainty', although as noted above we have actually translated it into a statistical uncertainty. There are no changes to the x_1 and c terms of the covariance and these are left unchanged from the original JLA analysis.

We show in the left-hand panel of Fig. 5 the square root of the diagonal entries of the peculiar velocities covariance matrix, translated into magnitude covariance, i.e. $\sigma_{m,ii}$ in equation (46). The right-hand panel shows the square root of the diagonal entries of the total magnitude covariance matrix (including all other magnitude uncertainties). Our values are compared with the original JLA values on the same figure. The largest difference in the total value of σ_m appears in the low redshift range, where our re-analysis modifies the associated peculiar velocities, which are dominant in this redshift range. In general, the net effect is to increase the statistical uncertainty while decreasing the systematic uncertainty with respect to the JLA analysis: at the median redshift of the low-z sample, $z = 0.0243$, the average diagonal σ_m due to statistical uncertainty in the peculiar velocities is 0.076 in our analysis (versus 0.045 JLA), while the
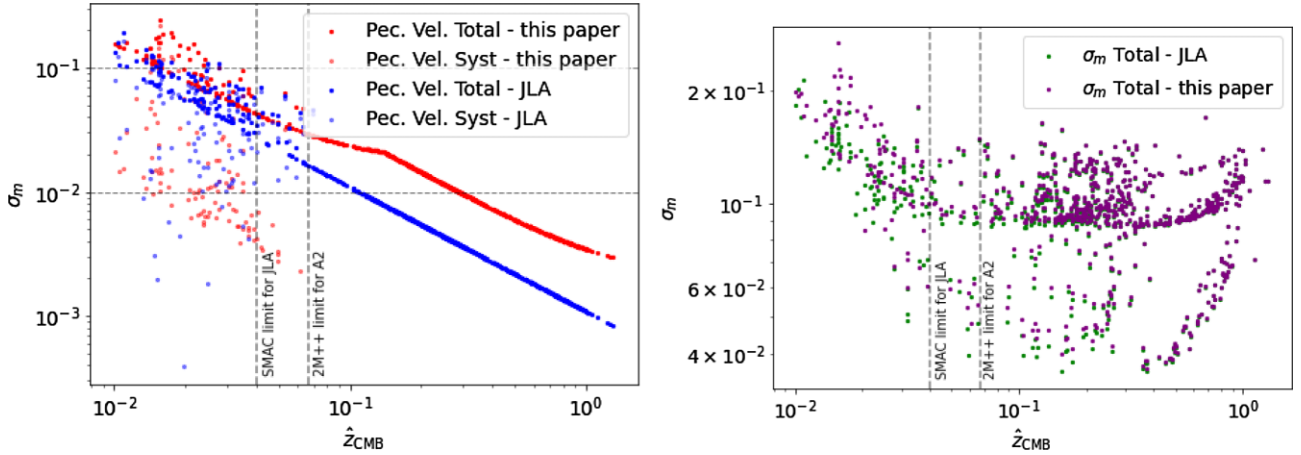
Figure 5. Left-hand panel: statistical and systematic (diagonal entries of the covariance matrix only) uncertainties in the apparent magnitude induced by peculiar velocity corrections for our re-analysis compared with JLA. Right-hand panel: total diagonal σ_m for our reanalysed and original JLA data. These components include the statistical error from the SALT2 fits and peculiar velocities as well systematics from several other components that are outlined in Betoule et al. (2014).

average systematic diagonal error is 0.020 in our work (versus 0.039 JLA). Overall, the total magnitude uncertainty due to peculiar velocities is increased by $\sim$30 per cent in our analysis (at the median redshift) compared to JLA. In the right-hand panel of Fig. 5, we compare the total uncertainties on the apparent magnitude (including all statistical and systematic uncertainties) between this work and the JLA analysis, showing that our magnitude uncertainties are generally larger, especially at low redshifts where the new peculiar velocity uncertainties dominate the error budget.

2.7 Choice of priors

As always in a Bayesian analysis, particular attention must be paid to priors, especially in the present case where we are interested in performing not only parameter inference but also model comparison (for an overview of the issue, see e.g. Trotta 2008).

The priors for the cosmological parameters $\mathscr{P}_1$ and for the other parameters in the hierarchical model are chosen as in Shariff et al. (2016), to which we refer for fuller details. A summary is provided in Table 1. For the cosmographic expansion parameters $\mathscr{P}_2$, the Uniform(0, 2) priors in Ω_m, Ω_Λ translate into the following non-uniform prior for the deceleration parameter $q_0 = \Omega_m/2 - \Omega_\Lambda$:

$$p(q_0) = \begin{cases} \frac{2}{3}(q+2) & \text{for } -2 \leq q_0 < -1, \\ 2/3 & \text{for } -1 \leq q_0 < 0, \\ \frac{2}{3}(1-q) & \text{for } 0 \leq q_0 \leq 1, \\ 0 & \text{otherwise.} \end{cases} \qquad (47)$$

Given that the likelihood's support is almost entirely within the region $-1.0 \lesssim q_0 \lesssim 0$, we choose the slightly simplified, uniform prior $q_0 \sim$ Uniform$(-2, 1)$. Since the jerk j_0 and spatial curvature Ω_κ appear in the degenerate combination $j_0 - \Omega_\kappa$ in the second-order term in the cosmographic expansion, equation (10), we adopt a uniform prior on this combination, with ranges motivated by the range of physically plausible curvature values.

The dipole amplitude parameter, D_μ, is a positive quantity for which the obvious choices of priors are a uniform or log-uniform prior. The lower boundary of the former is naturally 0, while for the latter a lower cutoff must be imposed in order for the prior to be

proper (i.e. normalizable). This however is problematic for the model selection outcome: as the likelihood becomes flat (i.e. insensitive to the value of D_μ) once D_μ drops below a certain threshold, the marginal posterior becomes equal to the marginal prior for arbitrarily lower values of D_μ with a log-uniform prior. This has an influence on the Bayes factor, as a larger prior range (i.e. a lower D_μ cut-off in a log-uniform prior) leads to a less favourable model selection outcome for the anisotropic model. In order to avoid this difficulty, we choose a uniform prior on D_μ itself. The upper prior cutoff is set by the characteristic scale expected by a dipole signal. This could be gleaned from a theoretical model, or, in a phenomenological approach such as ours, guided by the order of magnitude of previous upper limits on the parameter, which is of order $\sim 10^{-3}$. Such upper limits can however be considerably relaxed in the case of a dipole that is decaying with redshift, leading to upper limits of order $\sim 10^{-1}$ even when no dipole is present (see our simulated case of Fig. 8). In order to accommodate such a scenario, we choose a uniform prior $D_\mu \sim$ Uniform(0, 0.2).

We choose to sample the area of the sky in a uninformative manner since we do not have any prior belief of the directions a dipole might be pointing to. Requiring rotational invariance on the surface of the 2-sphere leads to a uniform distribution on the Galactic longitude of the dipole vector, $l_d \sim$ Uniform$(0, 2\pi)$ (in radians), and a uniform distribution on the cosine of the latitude of the dipole vector, $\cos(b_d) \sim$ Uniform[0, 1], with $b_d \in [0, \pi/2]$. Flipping the sign of b_d is equivalent to the transformation $l_d \rightarrow l_d + \pi \mod 2\pi$ and $D_\mu \rightarrow -D_\mu$. Hence in order to cover the possibility of a dipole pointing in a direction in the southern Galactic hemisphere, we extend the dipole amplitude to negative values, and therefore our prior is modified to $D_\mu \sim$ Uniform$(-0.2, 0.2)$. Similar considerations lead to a prior for the dipole amplitude on the deceleration parameter $D_{q_0} \sim$ Uniform$(-30, 30)$.

For the prior on the exponential scale parameter, S, we need to select a lower boundary (lest D_μ becomes unidentifiable and to stop pathologies associated with $S = 0$), which we take to be the scale of the lowest redshift SNe in our data, namely $S = 0.01$; for the upper boundary, we take $S = 0.1$ as it is known that the bulk flow does not disappear at least out to $z \sim 0.067$. In summary, our prior is thus $S \sim$ Uniform [0.01, 0.1].

3 SIMULATIONS AND TESTS OF METHODOLOGY

3.1 Simulated data

To test the ability of our setup to recover the anisotropy parameters within the BAHAMAS framework, we forward simulate data from our model in a similar manner to March et al. (2011), adding however JLA-like Galactic coordinates to our simulated SNe in order to carry out inference on a potential dipole. The fiducial values for the parameters are listed in Table 1. We consider a case with no dipole ($D_\mu = 0$) and a case with a large dipole ($D_\mu = 0.02$), pointing in the approximate direction of the CMB dipole and with an exponential scale, $S = 0.026$, matching the value preferred by the results of C19. The steps to generate the simulated data are as follows:

(i) Draw a value for the latent CMB restframe redshift, $z_{\mathrm{CMB},i}$, for each SNIa. z_{hel} is assumed to equal this CMB redshift. We draw 740 objects at the same redshifts as the real JLA data to ensure the binning of the data is the same when applying selection effects correction on simulated data as it is on real data. Notice that our simulations do not include the issue of peculiar velocity corrections, which are assumed to have already been performed.

(ii) Compute $\mu_i(\hat{z}, \Theta)$ using the fiducial values for our chosen cosmology, whether ΛCDM or the Cosmographic expansion.

(iii) Apply the dipolar modulation to the distance modulus using (14).

(iv) Draw the latent parameters x_{1i}, c_i, and M_i from the normal distributions, $x_{1i} \sim N(x_*, R_x^2)$, $c_i \sim N(c_*, R_c^2)$, and $M_i \sim N(M_0, \sigma_{\mathrm{res}}^2)$, respectively.

(v) Compute m_{Bi} using x_{1i}, c_i, M_i, and the Phillip's relation equation in (11).

(vi) Draw the value of the standard deviations $\sigma_{x_{1i}}$, σ_{c_i}, and σ_{m_i}, from the appropriate normal distributions fitted to the errors in the JLA data and use them to construct the 3×3 covariance matrix for each SNe as $C = \mathrm{diag}(\sigma_{c_i}^2, \sigma_{x_{1i}}^2, \sigma_{m_i}^2)$.

(vii) Draw the observed SALT2 parameters from $\hat{x}_{1i} \sim N(x_{1i}, \sigma_{x_{1i}}^2)$, $\hat{c}_i \sim N(c_i, \sigma_{ci}^2)$ and $\hat{m}_{Bi} \sim N(m_{Bi}, \sigma_{mi}^2)$.

(viii) Apply the selection function on the colour values drawn in the previous step. We use the values of $\sigma_{sj}^{\mathrm{obs}}$ and c_{sj}^{obs} inferred from the real JLA data in Section 2.4 for the redshift bins the SNIa falls in. If a given SNIa is not selected, we cycle back to step (iv) and redraw that SNIa. The process ends when all 740 objects are selected.

(ix) Generate positions for SNIa in the sky which match the positions of the JLA data. The non-isotropic distribution of the data has an effect on our ability to constrain a dipole, so it is important to match the real JLA SNIa positions for a realistic simulation.

An example of the simulated data, compared with the JLA data set, is shown in Figs 6 and 7, for a ΛCDM realization. Some banding of the data can be seen of the plots for σ_{x_1}, σ_c, and σ_{m_B}. This results from the different survey components comprising the JLA data. We can see that our simulated data does not capture this banding in the errors because we draw our errors from Gaussian distributions, but this approximation has no quantitative effect on our simulations. The well defined 'stripe' in the plot of the Galactic coordinates of the data is from the *SDSS* component of the JLA data.

We test the ability of our method to retrieve the true fiducial values listed in Table 1 from the simulated data under the seven different scenarios below:

(i) **ΛCDM-Isotropic** simulates an isotropic universe ($D_\mu = 0$) from ΛCDM and the inference also assumes a ΛCDM cosmology.

(ii) **ΛCDM-D** simulates a dipole ($D_\mu = 0.02$) with $F(z) = 1$ from ΛCDM and the inference also assumes a ΛCDM cosmology.

(iii) **ΛCDM-D-exp** simulates a dipole ($D_\mu = 0.02$) with $F(z) = \exp(-z/S)$ from ΛCDM and inference also assumes a ΛCDM cosmology, with the additional free parameter S.

(iv) **Cosmographic-Isotropic** simulates an isotropic universe ($D_\mu = 0$) from a cosmographic expansion and inference also assumes a cosmographic expansion.

(v) **Cosmographic-D** simulates a dipole with $F(z) = 1$ from a cosmographic expansions and inference also assumes a cosmographic expansion.

(vi) **Cosmographic-D-exp** simulates a dipole ($D_\mu = 0.02$) with $F(z) = \exp(-z/S)$ and inference also assumes a cosmographic expansion, with the additional free parameter S.

(vii) **Cosmographic-D-exp∗** simulates data as in ΛCDM-D-exp but the reconstruction adopts the cosmographic expansion instead. This serves to assess the bias in parameter reconstruction from the cosmographic expansion when the reconstruction model is miss-specified.

For each parametrization we generate 10 realizations of the data; each realisation contains 740 SNIa objects to be similar in size to the JLA data. The posterior results are averaged over the 10 realizations for each parametrization when we reconstruct the parameters in Section 3.2. We do not use the Gibbs sampler of Shariff et al. (2016) for posterior sampling, but rather adopt PyMultiNest (Buchner et al. 2014), an implementation of the Nested Sampling algorithm Multinest (Feroz & Hobson 2008; Feroz, Hobson & Bridges 2009; Feroz et al. 2019). The benefit is that we can also compute the Bayesian evidence which we will use for Bayesian model comparison in section 4.2.

3.2 Parameter Reconstruction from Simulations

We use BAHAMAS to construct posterior distributions (averaged over 10 data realizations) for the set of cosmological parameters $\mathscr{P}_1$ (i.e. ΛCDM) or $\mathscr{P}_2$ (i.e. cosmographic expansion) and anisotropy parameters $\{l_d, b_d, D_\mu, S\}$. Although they are sampled over during reconstruction, SNe population parameters and SALT2 coefficients are numerically marginalized over in corner plots and not visualized as they are not the focus of this paper. The difference between the 1D marginal posterior mean (averaged over realizations) and the true value of each parameter is displayed in Table 2. We observe that in all cases except for the scenario Cosmographic-D-exp∗ the difference is a fraction of a standard deviation, hence entirely within realization and sampling noise. The model misspecification of Cosmographic-D-exp∗, however, does lead to shifts of up to $\sim 1.4\sigma$ in the reconstructed cosmographic parameters, a reflection of the fact that the data have been generated under a different model, namely ΛCDM, than has been assumed in the reconstruction. However, the difference for the anisotropy parameters remains below 0.5σ.

It is instructive to investigate the expected constraints on the dipole amplitude when the simulated data are from a isotropic universe (scenario ΛCDM-Isotropic), shown in Fig. 8. The 1-sided 95 per cent upper limit we can place on D_μ for this simulated data is $D_\mu \leq 8.08 \times 10^{-4}$ (left-hand panel). When however we introduce the additional freedom of an exponential scale parameter S, the constraints in D_μ degrade by two orders of magnitude, as a small value of S confines any anisotropy to very small redshifts where the statistical power of our data is small and therefore degenerate with many values of D_μ which leads to the entire prior space on D_μ being well explored right up to the prior edge (right-hand panels of
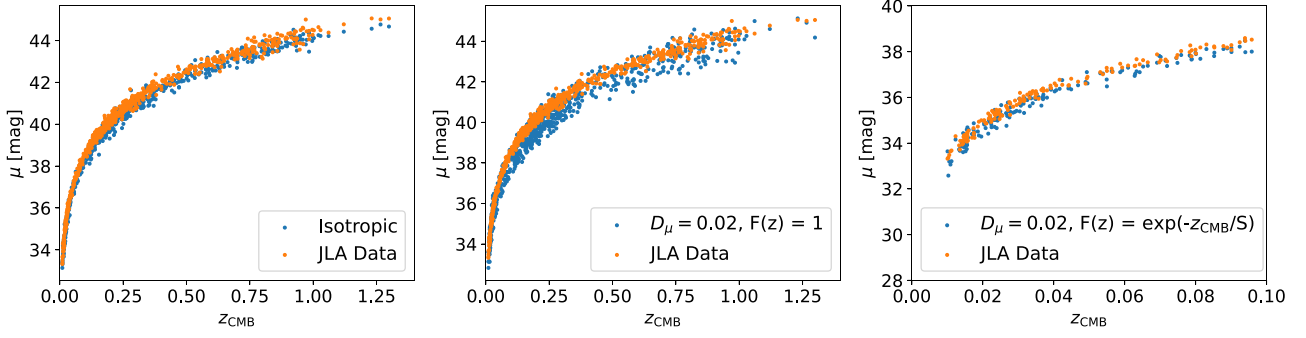
Figure 6. Simulated SNIa data generated using the JLA data set as a reference point. The simulations assume a ΛCDM model and no anisotropy in the distance modulus for the left most model. A dipole of value $D_\mu = 0.02$ is present for the second plot. The third plot also has this value of the dipole, but restricted to a local scale ($z \sim 0.1$) by multiplying the dipole term by the function $F(z) = \exp(-z/0.026)$. For this third plot, the redshift has been truncated to only show the redshift range where the dipole is noticeable.
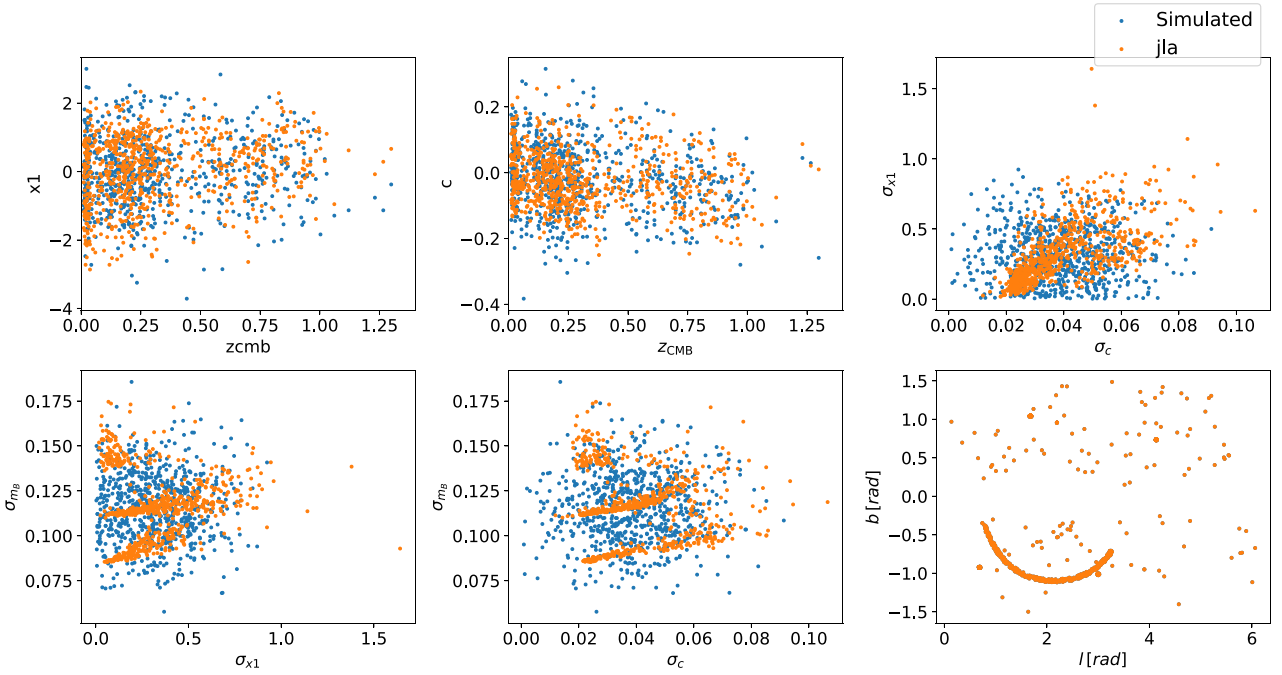

Figure 7. Simulated SNIa data generated using the JLA data set as a reference point, assuming ΛCDM as a fiducial model: distribution of colour (c), stretch (x_1), and the respective standard deviation entering the observational error covariance matrix, as well as the SNIa's sky coordinates.

Table 2. Difference between the 1D marginal posterior mean and the true value used to simulated JLA-data, averaged over 10 data realizations each, $\Delta x \equiv x_{\text{true}} - \bar{x}$ for each parameter x. In parenthesis, the difference is expressed in units of the 1D posterior standard deviation. The top (middle) section shows the case where ΛCDM (Cosmographic expansion) is assumed both for the simulation and the inference; the bottom row assumes ΛCDM for the simulation and the Cosmographic expansion for the inference – a case of model miss-specification.

| Model	Δq_0	$\Delta(j_0 - \Omega_\kappa)$	$\Delta\Omega_M$	$\Delta\Omega_\Lambda$	Δl(rad)	Δb(rad)	$\lvert\Delta D_\mu\rvert(\times 10^{-2})$	$\Delta S(\times 10^{-2})$
			Simulation: ΛCDM; reconstruction: ΛCDM					
(ia) ΛCDM-Isotropic, $F(z) = 0$	–	–	$0.03(0.51\sigma)$	$0.05(0.36\sigma)$	–	–	$<1.00 \times 10^{-1}(2\sigma)$	–
(ib) ΛCDM-Isotropic, $F(z) = \exp(-z/S)$	–	–	$0.03(0.51\sigma)$	$0.05(0.36\sigma)$	–	–	$<4.96 \times 10^{-1}(2\sigma)$	$<9.29(2\sigma)$
(ii) ΛCDM-D	–	–	$-0.02(0.19\sigma)$	$0.02(0.10\sigma)$	$-0.003(0.20\sigma)$	$-0.003(0.25\sigma)$	$0.036(0.13\sigma)$	–
(iii) ΛCDM-D-exp	–	–	$0.03(0.91\sigma)$	$0.07(0.72\sigma)$	$0.02(0.20\sigma)$	$-0.02(0.17\sigma)$	$-0.16(0.28\sigma)$	$-0.10(0.21\sigma)$
			Simulation: Cosmographic; reconstruction: Cosmographic					
(iv) Cosmographic-Isotropic, $F(z) = 0$	$-0.02(0.20\sigma)$	$0.03(0.01\sigma)$	–	–	–	–	–	–
(v) Cosmographic-D	$-0.06(0.56\sigma)$	$0.27(0.58\sigma)$	–	–	$-0.0116(0.37\sigma)$	$-0.003(0.26\sigma)$	$-0.01(0.35\sigma)$	–
(vi) Cosmographic-D-exp	$-0.01(0.10\sigma)$	$-0.05(0.14\sigma)$	–	–	$-0.04(0.20\sigma)$	$0.01(0.08\sigma)$	$-0.13(0.30\sigma)$	$0.16(0.37\sigma)$
			Simulation: ΛCDM; reconstruction: Cosmographic					
(vii) Cosmographic-D-exp	$-0.11(1.05\sigma)$	$-0.63(1.37\sigma)$	–	–	$0.11(0.60\sigma)$	$0.038(0.37\sigma)$	$-0.128(0.44\sigma)$	$-0.165(0.24\sigma)$
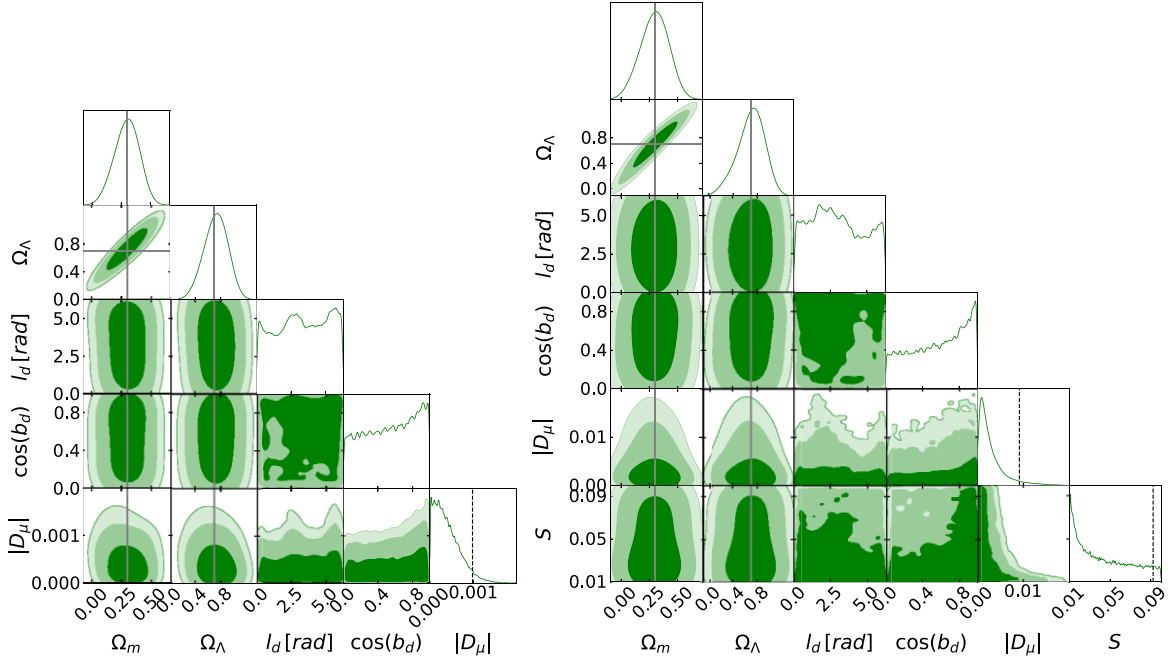
Figure 8. Posterior distributions from simulated JLA-like data, averaged over 10 data realizations. The simulations assume a ΛCDM isotropic universe ($D_\mu = 0$); the reconstructions allow for a dipole in the distance modulus with $F(z) = 1$ (left) and $F(z) = \exp(-z/S)$ (right). Contours in 2D plots enclose joint 1σ, 2σ, and 3σ highest posterior density (HPD) credible regions; the vertical dashed line in the 1D marginals for D_μ and S delimits the 2σ upper limit. Notice the different scales in the axis of D_μ between the two cases.

Fig. 8.). The 95 per cent upper bound becomes $D_\mu < 4.36 \times 10^{-2}$ and $S < 4.56 \times 10^{-2}$. Qualitatively similar results apply for the Cosmographic expansion.

The above simulations do not include colour-based selection effects for simplicity. A simulation study including colour-based selection appears in Appendix A (see Fig. A2) and shows that averaging the posterior distributions across replicates yields 2D and 1D marginal distributions that are centered on the true values of the parameters.

4 RESULTS

4.1 Parameter Inference

We begin by presenting the impact of our new treatment of peculiar velocities and colour selection effects correction on the constraints on Ω_m, Ω_Λ for the case of an isotropic universe, as shown in Fig. 9. In the left-hand panel, we compare the constraints using the old JLA peculiar velocities and $z_{\rm CMB}$ as in Betoule et al. (2014) (green) to the ones obtained using our new, group-corrected values of the CMB rest-frame redshifts (blue), and additionally replacing the JLA peculiar velocities with our newly derived ones (orange). The constraints on the parameters of our models from JLA data are summarized in Table 3, for both the ΛCDM model and the Cosmographic expansion. In the top section we also investigate the impact of our newly derived values for $z_{\rm CMB}$, peculiar velocity corrections and colour-based selection effects on Ω_m, Ω_Λ constraints in an isotropic universe. Starting from the same treatment as Betoule et al. (2014), we find $\Omega_m = 0.306 \pm 0.087$, in good agreement with the value in Betoule et al. (2014), $\Omega_m = 0.295 \pm 0.034$ but with significantly larger uncertainty, perhaps on account of the different statistical approach. When replacing the CMB rest-frame redshifts used in Betoule et al.

(2014) with the ones presented here, we find $\Omega_m = 0.253 \pm 0.089$, a shift of about half a standard deviation according to our uncertainty, but of 1.5σ in units of the standard deviation quoted by Betoule et al. (2014). The effect of using the new peculiar velocity corrections (with their newly derived associated covariance matrix) while maintaining the value of CMB rest-frame redshift from Betoule et al. (2014) results in a more modest shift, $\Omega_m = 0.297 \pm 0.089$ (case 2M++, old $z_{\rm CMB}$). When using both the new redshift values and our newly derived peculiar velocity corrections in combination, we obtain $\Omega_m = 0.273 \pm 0.090$. All these results do not use our new colour-based selection effects corrections; once those are included, the constraint on the matter density shifts back to a value close to the original JLA analysis, namely $\Omega_m = 0.290 \pm 0.091$ (but notice the larger uncertainty on our result).

In the right-hand panel of Fig. 9, we observe a shift in the posterior towards lower Ω_Λ and larger Ω_m when adding the systematic covariance matrix (including our new peculiar velocity covariances) to the statistical covariance matrix, as already noticed by Shariff et al. (2016). Further adding the correction for colour selection effects shifts the posterior only slightly.

The second section of Table 3 presents our constraints on the distance modulus dipole parameters, also comparing the impact of using the colour selection effect correction (as indicated in the third column), which is found to be quite minor on all constraints. Posterior 1D and 2D distributions are shown in Fig. 10 for the ΛCDM model and in Fig. 11 for the Cosmographic expansion. The posterior distribution for the dipole $|D_\mu|$ in the left-hand panel of Fig. 10 for the ΛCDM model with $F(z) = 1$ peaks at 0, and we set a 1-tailed 95 per cent upper bound of $|D_\mu| < 5.93 \times 10^{-4}$ (95.45 per cent probability) – a factor of ~ 2 tighter than the limits derived by Lin et al. (2016a) from the same data, namely $|D_\mu| < 1.98 \times 10^{-3}$ (see Table 4). The dipole direction is correspondingly unconstrained.
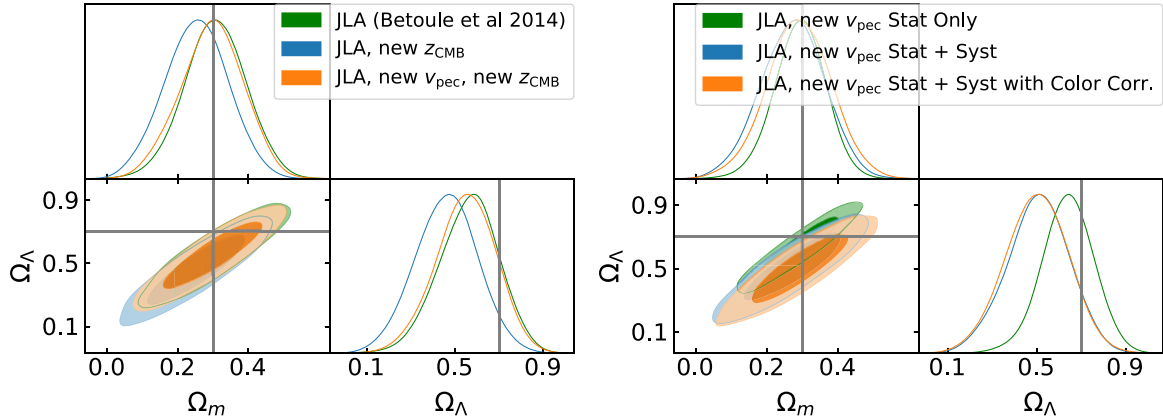
Figure 9. Impact of our new treatment of peculiar velocities and colour selection effects correction on the constraints on Ω_m, Ω_Λ for the case of an isotropic universe. Left-hand panel: comparison of marginal posteriors Ω_m, Ω_Λ using the old JLA peculiar velocity uncertainties and z_{CMB} (green) to the ones obtained using our new, group-corrected values of the CMB rest-frame redshifts (blue), and additionally replacing the JLA peculiar velocity uncertainties with our newly derived ones (orange). Right-hand panel: posterior using only the statistical covariance matrix (green), adding the systematic covariance matrix (including our new peculiar velocity covariances, blue) and further adding colour selection effects corrections (orange). In this panel, we adopt our newly derived, group-corrects CMB rest-frame redshifts.

In the second case, shown in the right-hand panel of Fig. 10, a scale function of the form $F(z) = \exp(-z/S)$ is used to constrain the dipole to local region. As expected from our simulations, we find a degeneracy between the dipole parameter and its scale, whose effect is to degrade the upper limits on the dipole amplitude to $|D_\mu| < 1.05 \times 10^{-2}$ for the ΛCDM case. We can see $|D_\mu|$ is well explored again, right up to its prior edge because of this degeneracy, which contributes to these weaker constraints. The limits on the dipole scale S are also weak, with the 1D marginal distribution stretching all the way to the prior boundary ($S = 0.10$), but peaking near the lower prior boundary. The very weak preference for a non-zero dipole (seen in the peak away from 0 in the 1D marginal distribution) could be an indication of a residual effects of the bulk flow, which points broadly in the same direction as the more prominent peak in the l_d posterior distribution. Such departures from perfect isotropy are weak, and not dissimilar from what we observed in our isotropic universe simulations (Fig. 8, right-hand panel) – hence they can be easily ascribed to the result of random noise. With regards to constraints on cosmological parameters, with respect to the ΛCDM-Isotropic case, we observe only a very mild shift in their value as a consequence of the introduction of a potential dipole in the model, $|\Delta\Omega_M| = 0.005$ and $|\Delta\Omega_\Lambda| = 0.006$. Both are shifts of less than 0.1 standard deviations of the posterior, and are similar in scale for the case with $F(z) = 1$. A similar result is seen in the Cosmographic case with $|\Delta q_0| = 0.009$ which is also quite minor relative to the posterior standard deviation.

For the isotropic Cosmographic expansion, the posterior mean for the deceleration parameter increases from $q_0 = -0.352 \pm 0.092$ when using the old PSCz velocity corrections and z_{CMB} to $q_0 = -0.302 \pm 0.090$ when updating both velocity corrections and CMB rest-frame redshifts to the new values we derived here (the error indicates the standard deviation of the posterior, not the uncertainty on the mean). When introducing the possibility of a dipole, the posterior mean for q_0 hovers around -0.30, depending on the dipole model and whether we adopt the colour selection effects corrections. These values are quite a bit larger than the expectation under ΛCDM, namely $q_0 = -0.55$, but not as large as the results reported in table 2 of Colin et al. (2019b) ($q_0 = -0.157$ in our notation), who ascribed

the shift of the deceleration parameter towards 0 to evidence for an anisotropic universe. Our analysis (with its improved treatments of peculiar velocities and colour selection effects) disagrees with those conclusions: the marginal posterior probability (obtained from our posterior samples, not a Gaussian approximation to the posterior) for $q_0 \geq 0$ (i.e. no acceleration) for the $F(z) = 1$ case with selection effects corrections and a distance modulus dipole is 9.3×10^{-4}. We return on this question from the point of view of Bayesian model comparison in Section 4.2.

The constraints on the dipole parameters for the Cosmographic expansion model are qualitatively similar to those presented for the ΛCDM model, as shown in Fig. 11 and detailed in the central two sections of Table 3. For the $F(z) = 1$ case, the posterior dipole amplitude peaks at 0 and we set a 95 per cent upper limit $|D_{q_0}| < 6.32 \times 10^{-4}$. There is no significant evidence for a dipole moment in the Cosmographic expansion case under our data and models. A qualitatively similar picture holds for the $F(z) = \exp(-z/S)$ case, albeit with weaker limits on the dipole amplitude owing to the degeneracy with the scale parameter S.

For a more direct comparison with the results of C19, we have also investigated the same model as C19, where the dipole modulation is applied to the deceleration parameter q_0, as in equation (15), rather than to the distance modulus μ. Differently from C19, we did *not* remove the bias corrections to the magnitude, we kept the direction of the dipole free (as opposed to being fixed in the CMB dipole direction), used our new peculiar velocity corrections and CMB rest-frame redshifts (as opposed to heliocentric redshifts) and applied our new colour selection effects. The resulting posteriors are shown in Fig. 12 and constraints presented in the bottom section of Table 3.

We see qualitatively similar results to the case where we model the dipole on q_0 in the Cosmographic expansion. For the $F(z) = 1$ case, the posterior dipole amplitude again peaks at 0 and we set a 95 per cent upper limit $|D_{q_0}| < 6.29 \times 10^{-2}$. A qualitatively similar picture holds for the $F(z) = \exp(-z/S)$ case with a preference for a small S value. This is in contrast with Colin et al. (2019b), who saw a preference of a scale value $S = 0.0262$, a likely consequence of their removal of peculiar velocity correction and the use of heliocentric redshifts.

Table 3. Parameter constraints from 1D marginal posterior distributions from JLA data, and outcome of Bayesian model comparison (last column) for the models and data considered. The second column indicates the peculiar velocity corrections adopted: 'PSCz' is the same treatment as in Betoule et al. (2014); '2M++' indicates the new treatment in this paper; 'PSCz, new z_{CMB}' uses the peculiar velocity corrections of Betoule et al. (2014) but our newly derived CMB rest-frame redshift, while '2M++, old z_{CMB}' uses our newly derived peculiar velocity corrections but the same z_{CMB} as Betoule et al. (2014). The last column is the difference between the model's log-evidence and log-evidence of the ΛCDM-Isotropic or Cosmographic-Isotropic case (with or without colour correction, as appropriate), i.e. the log of the Bayes factor. A negative value indicates that the model under consideration is disfavoured w.r.t. the isotropic universe. The ⋆ on some of the data for $\Delta\ln(Z)$ are to indicate that the calculation involved a comparison for a Cosmographic expansion with a restricted prior on the deceleration parameter of $q_0 \sim [-2, 0)$ which limits it to an accelerating universe only.

Model	v_{pec}^{SN} correction	Selection correction	Ω_m	Ω_Λ	l_d (rad)	b_d (rad)	$\lvert D_{\mu,l}\rvert$	Dipole scale, S	Quantity modulated	$\Delta\ln(Z)$
ΛCDM-Isotropic	PSCz	No	0.306 ± 0.087	0.562 ± 0.135	–	–	–	–	–	
ΛCDM-Isotropic	PSCz, new z_{CMB}	No	0.253 ± 0.089	0.460 ± 0.139	–	–	–	–	–	
ΛCDM-Isotropic	2M++, old z_{CMB}	No	0.297 ± 0.089	0.547 ± 0.137	–	–	–	–	–	0.0
ΛCDM-Isotropic	2M++	No	0.273 ± 0.090	0.508 ± 0.140	–	–	–	–	–	0.0
ΛCDM-Isotropic	2M++	Yes	0.290 ± 0.091	0.500 ± 0.141	–	–	–	–	–	
CDM only-Isotropic	2M++	No	0.037 ± 0.028	0	–	–	–	–	–	-5.65
CDM only-Isotropic	2M++	Yes	0.037 ± 0.028	0	–	–	–	–	–	-4.85
ΛCDM-D	2M++	No	0.263 ± 0.090	0.493 ± 0.140	Unconstrained	Unconstrained	$< 5.75 \times 10^{-4}$ (95 per cent)	–	μ	-8.68 ± 0.01
ΛCDM-D	2M++	Yes	0.285 ± 0.094	0.490 ± 0.143	Unconstrained	Unconstrained	$< 5.93 \times 10^{-4}$ (95 per cent)	–	μ	-6.81 ± 0.01
ΛCDM-D-Exp	2M++	No	0.269 ± 0.087	0.499 ± 0.137	Unconstrained	Unconstrained	$< 9.81 \times 10^{-3}$ (95 per cent)	$< 8.75 \times 10^{-2}$ (95 per cent)	μ	-5.27 ± 0.08
ΛCDM-D-Exp	2M++	Yes	0.286 ± 0.091	0.487 ± 0.142	Unconstrained	Unconstrained	$< 1.05 \times 10^{-2}$ (95 per cent)	$< 8.71 \times 10^{-2}$ (95 per cent)	μ	-3.49 ± 0.01
→	→	→	q_0	$j_0 - \Omega_\kappa$	→	→	→	→	→	→
Cosmographic-Isotropic	PSCz	No	-0.352 ± 0.092	0.114 ± 0.391	–	–	–	–	–	
Cosmographic-Isotropic	PSCz, new z_{CMB}	No	-0.288 ± 0.095	-0.132 ± 0.370	–	–	–	–	–	
Cosmographic-Isotropic	2M++, old z_{CMB}	No	-0.342 ± 0.093	0.071 ± 0.390	–	–	–	–	–	0.0
Cosmographic-Isotropic	2M++	No	-0.320 ± 0.094	-0.254 ± 0.383	–	–	–	–	–	0.0
Cosmographic-Isotropic	2M++	Yes	-0.302 ± 0.090	-0.023 ± 0.357	–	–	–	–	–	
Cosmographic-($q_0 = 0$)	2M++	No	0	-0.953 ± 0.140	–	–	–	–	–	$-3.90 \pm 0.06^*$
Cosmographic-($q_0 = 0$)	2M++	Yes	0	-0.881 ± 0.134	–	–	–	–	–	$-3.28 \pm 0.09^*$
Cosmographic-($q_0 \geq 0$)	2M++	No	$< 0.067 \times 10^{-2}$ (95 per cent)	-0.922 ± 0.141	–	–	–	–	–	$-7.39 \pm 0.05^*$
Cosmographic-($q_0 \geq 0$)	2M++	Yes	$< 0.074 \times 10^{-2}$ (95 per cent)	-0.922 ± 0.144	Unconstrained	Unconstrained	–	–	–	$-7.00 \pm 0.09^*$
Cosmographic-D	2M++	No	-0.307 ± 0.093	-0.085 ± 0.375	Unconstrained	Unconstrained	$< 6.43 \times 10^{-4}$ (95 per cent)	–	μ	-6.36 ± 0.02
Cosmographic-D	2M++	Yes	-0.291 ± 0.095	-0.070 ± 0.371	Unconstrained	Unconstrained	$< 6.32 \times 10^{-4}$ (95 per cent)	–	μ	-6.47 ± 0.02
Cosmographic-D-Exp	2M++	No	-0.307 ± 0.089	-0.069 ± 0.353	Unconstrained	Unconstrained	$< 1.00 \times 10^{-2}$ (95 per cent)	$< 8.68 \times 10^{-2}$ (95 per cent)	μ	-2.96 ± 0.05
Cosmographic-D-Exp	2M++	Yes	-0.293 ± 0.094	-0.048 ± 0.362	Unconstrained	Unconstrained	$< 9.63 \times 10^{-3}$ (95 per cent)	$< 8.94 \times 10^{-2}$ (95 per cent)	μ	-3.26 ± 0.01
→	→	→	q_0	$j_0 - \Omega_\kappa$	→	→	$\lvert D_q \rvert$	→	→	→
Cosmographic-D	2M++	No	-0.305 ± 0.094	-0.083 ± 0.376	Unconstrained	Unconstrained	$< 6.06 \times 10^{-2}$ (95 per cent)	–	q_0	-7.12 ± 0.02
Cosmographic-D	2M++	Yes	-0.286 ± 0.094	-0.084 ± 0.367	Unconstrained	Unconstrained	$< 6.29 \times 10^{-2}$ (95 per cent)	–	q_0	-7.45 ± 0.08
Cosmographic-D-Exp	2M++	No	-0.316 ± 0.097	-0.040 ± 0.370	Unconstrained	Unconstrained	< 22.46 (95 per cent)	$< 5.59 \times 10^{-2}$ (95 per cent)	q_0	-1.22 ± 0.02
Cosmographic-D-Exp	2M++	Yes	-0.296 ± 0.093	-0.043 ± 0.359	Unconstrained	Unconstrained	< 23.4595 per cent	$< 6.00 \times 10^{-2}$ (95 per cent)	q_0	-1.42 ± 0.02

Table 4. Comparison of our results with previous searches for a dipolar modulation. We only include comparable results that utilize the 'dipole fitting' approach (as opposed to the 'hemisphere comparison' method). Reported detections (at higher than 95 per cent significance) are highlighted in boldface. The third column 'v_{pec} corr' states whether peculiar velocity corrections were adopted, and if so from which data set they were derived. It should be noted here, previous significant detections involved data that had no peculiar velocity corrections.

| Reference	Data	v_{pec} corr	l_d (deg)	b_d (deg)	Dipole amplitude	Quantity modulated
Cooke & Lynden-Bell (2010)	Union	None	309	43	0.14 ± 0.12	d_L
Lin, Li & Chang (2016b)	Union2.1	None	$171.8^{+42.0}_{-42.0}$	$9.9^{+20.3}_{-20.3}$	0.160 ± 0.115	Ω_m
Mariano & Perivolaropoulos (2012)	Union2	**None**	309^{+18}_{-18}	$-15.1^{+11.5}_{-11.5}$	$\mathbf{(1.3 \pm 0.6) \times 10^{-3}}$	μ
Yang, Wang & Chu (2014)	Union2.1	**None**	$307.1^{+16.2}_{-16.2}$	$-14.3^{+10.1}_{-10.1}$	$\mathbf{(1.2 \pm 0.5) \times 10^{-3}}$	μ
Wang & Wang (2014)	Union2.1+GRB	**None**	$309.2^{+15.8}_{-15.8}$	$-8.6^{+10.5}_{-10.5}$	$\mathbf{(1.37 \pm 0.57) \times 10^{-3}}$	μ
Lin et al. (2016a)	JLA	PSCz	316^{+107}_{-110}	-5^{+41}_{-60}	$<1.98 \times 10^{-3}$ (95 per cent)	μ
Sun & Wang (2018a)	Union2.1	**None**	$309^{+15.5}_{-15.7}$	$-8.9^{+11.2}_{-9.8}$	$\mathbf{(1.46 \pm 0.56) \times 10^{-3}}$	μ
Sun & Wang (2018a)	Constitution	None	$67.0^{+66.5}_{-66.2}$	$-0.6^{+25.2}_{-26.3}$	$(4.4 \pm 5.0) \times 10^{-4}$	μ
Sun & Wang (2018a)	JLA	PSCz	Unconstrained	Unconstrained	Unconstrained	μ
Sun & Wang (2018b)	Pantheon	2M++	329^{+101}_{-28}	37^{+52}_{-21}	$(3.7^{+2.5}_{-3.7}) \times 10^{-4}$ (95 per cent)	μ
Zhao et al. (2019)	Pantheon	2M++	$306.00^{+82.95}_{-125.01}$	$-34.20^{+16.82}_{-54.93}$	$<1.16 \times 10^{-4}$ (95 per cent)	μ
This work	JLA	2M++	Unconstrained	Unconstrained	$<5.93 \times 10^{-4}$ (95 per cent)	$\mu, F(z) = 1$
This work	JLA	2M++	Unconstrained	Unconstrained	$<1.05 \times 10^{-2}$ (95 per cent)	$\mu, F(z) = \exp(-z/S)$
Colin et al. (2019b)	JLA	**None**	264.021 (fixed)	48.253 (fixed)	$\mathbf{-8.03^{+2.05}_{-2.05}}$	$q_0, F(z) = \exp(-z/S)$
Rubin & Heitlauf (2020)	JLA	**None**	264.021 (fixed)	48.253 (fixed)	$-8.65^{+2.2}_{-2.6}$	$q_0, F(z) = \exp(-z/S)$
Rubin & Heitlauf (2020)	JLA	PCSz	264.021 (fixed)	48.253 (fixed)	$-1.1^{+3.2}_{-3.4}$	$q_0, F(z) = \exp(-z/S)$
This work	JLA	2M++	Unconstrained	Unconstrained	$<6.32 \times 10^{-2}$ (95 per cent)	$q_0, F(z) = 1$
This work	JLA	2M++	Unconstrained	Unconstrained	<13.68 (95 per cent)	$q_0, F(z) = \exp(-z/S)$
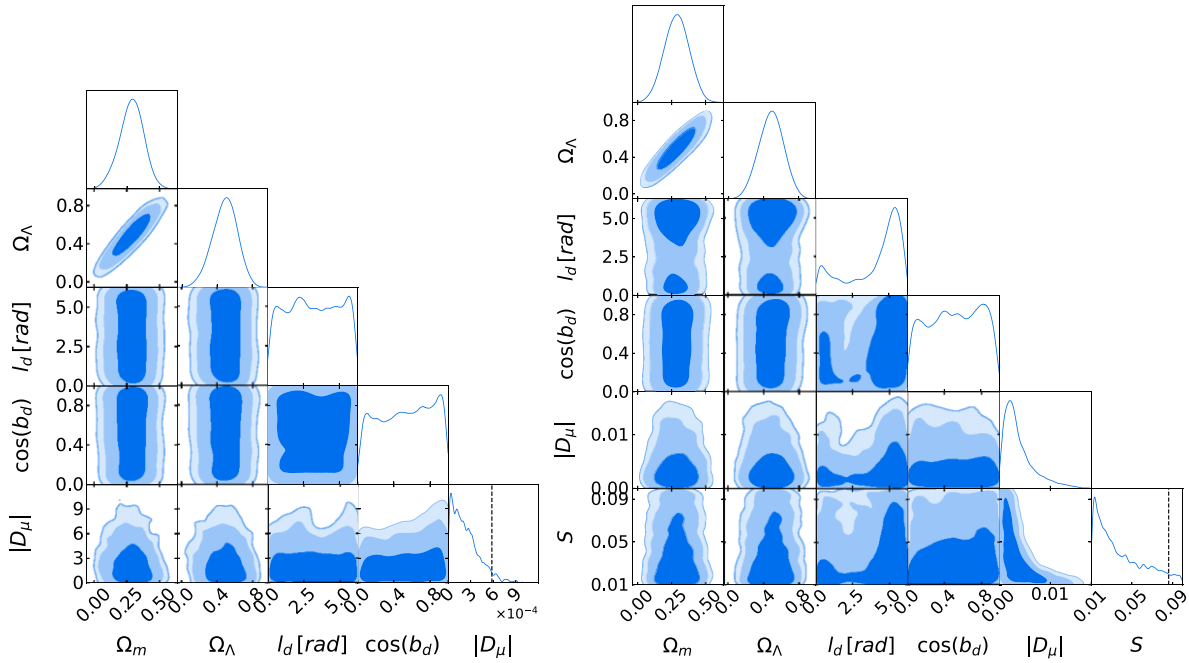
Figure 10. Posterior inference allowing for a distance modulus dipole from JLA data, assuming the ΛCDM model with $F(z) = 1$ (left) and $F(z) = \exp(-z/S)$ (right), including colour-based selection effects correction. Contours in 2D plots enclose joint 1σ, 2σ, and 3σ HPD credible regions; the vertical dashed line in the 1D marginals for D_μ and S delimits the 2σ upper limit.
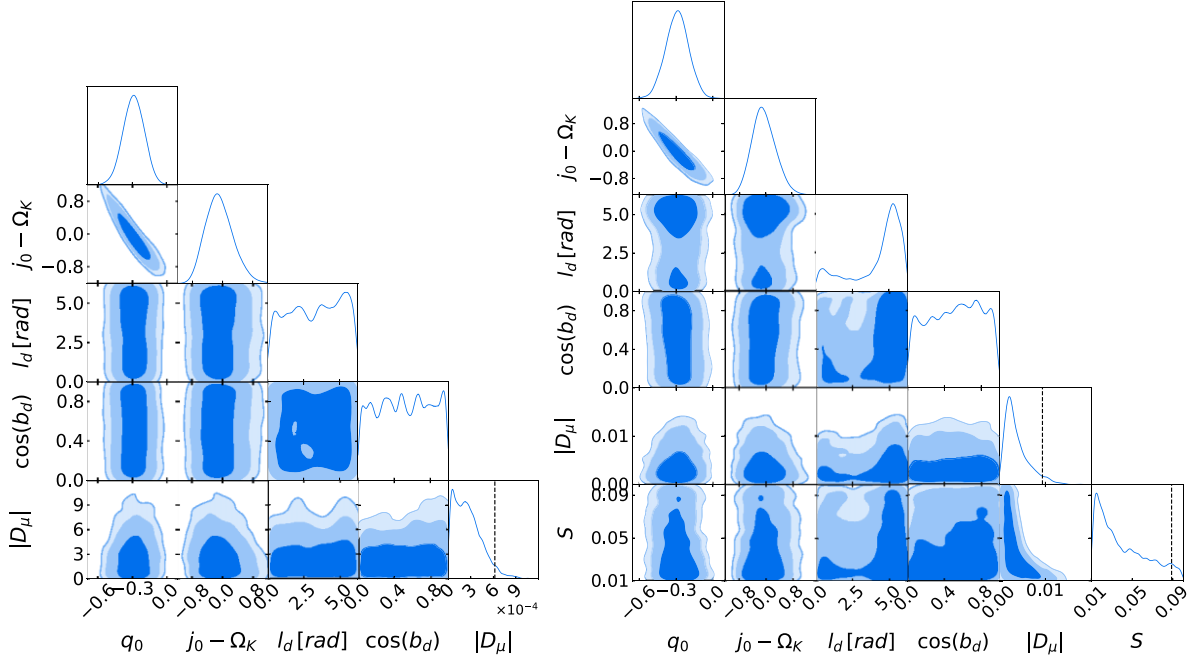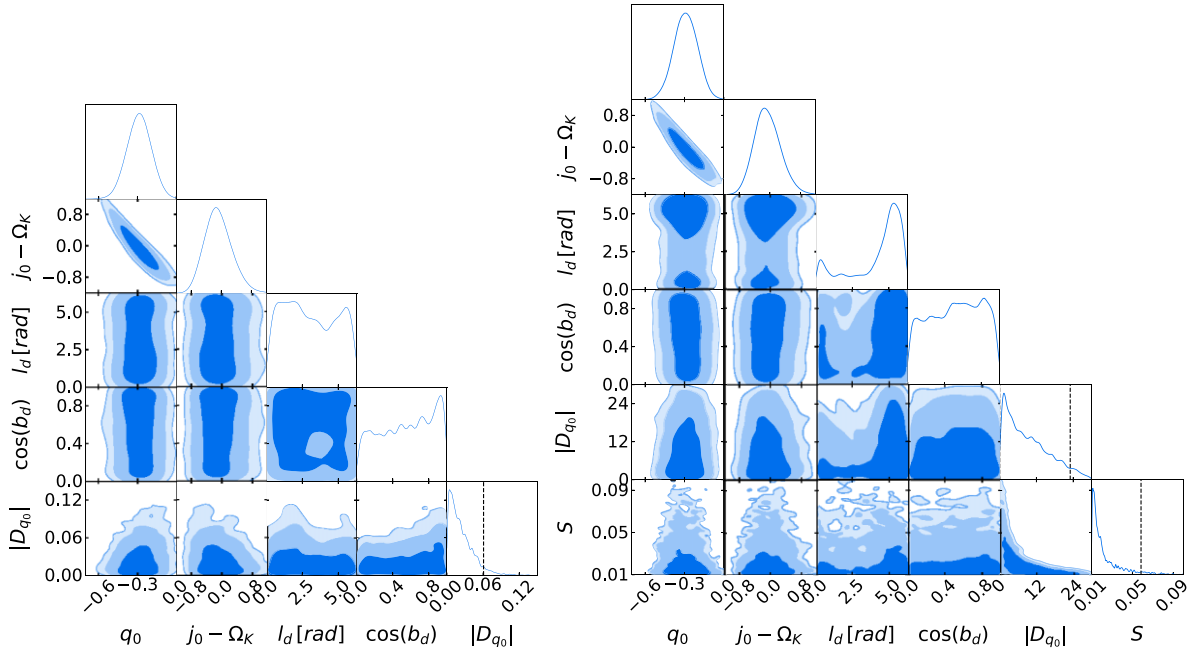
Figure 11. Posterior inference allowing for a distance modulus dipole from JLA data, assuming the Cosmographic expansion model with $F(z) = 1$ (left) and $F(z) = \exp(-z/S)$ (right), including colour-based selection effects correction. Contours in 2D plots enclose joint 1σ, 2σ, and 3σ HPD credible regions; the vertical dashed line in the 1D marginals for D_μ and S delimits the 2σ upper limit.

Figure 12. Posterior inference allowing for a distance modulus dipole from JLA data, assuming the Cosmographic expansion model with $F(z) = 1$ (left) and $F(z) = \exp(-z/S)$ (right), including colour-based selection effects correction. Contours in 2D plots enclose joint 1σ, 2σ, and 3σ HPD credible regions; the vertical dashed line in the 1D marginals for D_{q_0} and S delimits the 2σ upper limit. The dipole here is modelled directly on the deceleration parameter rather than the distance modulus, similar to C19.

4.2 Bayesian model comparison

We compare the isotropic expansion model to the alternatives featuring a dipole via Bayesian model comparison, and report the difference in the log of the Bayesian evidence (i.e. the log of the Bayes factor) in Table 3:

$$\Delta \ln(Z) = \ln B_D - \ln B_I, \tag{48}$$

where B_I is the Bayesian evidence for the isotropic model (either

ΛCDM or Cosmographic expansion) and B_D is the evidence for a model featuring a dipole, with priors as in Table 1. A value of $\Delta \ln (Z) < 0$ indicates a preference for the isotropic model. According to the Jaynes' scale for the strength of evidence, values of $|\Delta \ln (Z)| = 2.5(5.0)$ correspond to moderate (strong) evidence for one of the models being compared. For equal prior probability for the models, the quantity $\exp (\Delta \ln (Z)) = B_D/B_I$ gives the posterior odds between the isotropic and the dipole expansion models, which are approximately 12:1 (150:1) for moderate (strong) evidence [see Trotta (2008) for details on Bayesian model comparison]. When considering the numerical odds derived from the Bayesian evidence, it is important to bear in mind that these can be very sensitive to the choice of prior distribution, particularly the prior on the parameters that only appears in the more complicated model (i.e. the model featuring the dipole). While we believe that our choices of prior distributions are well justified in Section 2.7, researchers that make other choices for their prior distributions may compute odds ratios that differ from those that we report.

In Table 1 we only carry out pair-wise model comparisons between models that use the same data and same treatment of colour selection effects, for comparing models with different data and/or assumptions about the data generating process would be meaningless. The evidences (and associated uncertainties) are estimated with `PyMultinest`, which was run with 400 live points and an evidence tolerance of 0.5. We observe that the isotropic model is favoured over all others: in the ΛCDM scenario, the constant dipole model is disfavoured with odds ranging from 900:1 to almost 6000:1, depending on the adoption of colour selection effects. The model with a dipole falling off with redshift is also disfavoured, albeit with smaller odds ranging between 32:1 and 194:1.

A similar pictures holds for comparison between models in the Cosmographic expansion case. Here, the odds against the anistropic models are generally smaller than in ΛCDM, owing to the smaller parameter space volume ratio between posterior and prior, which control the strength of the Occam's razor effect in favour of the isotropic model. We also note that when introducing a dipole scale parameter S, despite the larger number of free parameters in this model w.r.t. the case where the dipole is constant in redshift, the Bayes factor against it is actually smaller than the constant-in-redshift dipole case. This can be explained by noting that the introduction of S as a free parameter leads to much less stringent limits on the dipole amplitude because of the degeneracy explained above. Since S itself is only weakly constrained, the Occam's razor effect for these two parameters is weakened, leading to a weaker preference for the isotropic model. As a consequence, the Cosmographic-D-Exp model where the dipole is on the deceleration parameter is only very mildly disfavoured (odds smaller than 5:1) w.r.t. the isotropic model – a consequence of the fact that the additional parameters for this model cannot be strongly constrained, and hence the posterior odds remain approximately equal to the prior odds.

As another case, we reproduce the setup used in C19, namely removing peculiar velocity corrections entirely, using heliocentric redshifts [i.e. z_{hel} instead of $\bar{z}$ in equation (34), a choice that imprints the dipole due to the Solar system's motion on to the data, as pointed out by Rubin & Heitlauf (2020)] and removing from the covariance matrix all uncertainties associated with peculiar velocity corrections. In this setup, we compare the evidence for an isotropic Cosmographic expansion with that of a dipolar modulation of the form $F(z) = \exp (-z/S)$ either on the deceleration parameter, equation (15) (as in C19), or on the distance modulus, equation (14). We adopt a Gaussian prior with a standard deviation of $10°$ on the dipole direction, centred on the bulk flow direction from Boruah et al. (2020), namely $l_{bf} =$ $301° \pm 4°$, $b_{bf} = 0° \pm 3°$ (in excellent agreement with the results of Said et al. (2020), obtained using the Fundamental–Plane relation, namely $l_{bf} = 304° \pm 4°$, $b_{bf} = 1° \pm 4°$). When the dipole is modelled on the deceleration parameter, as in C19, the Cosmographic anisotropic model is still disfavoured with respect to the isotropic one, with odds of approximately 17:1 ($\Delta \ln (Z) = -2.84 \pm 0.08$). Although the anisotropic model achieves a better quality of fit by absorbing the dipole in the data, from an Occam's razor perspective it remains disfavoured due to its additional, unwarranted model complexity. We observe a similar effect (if stronger) when the dipole is modelled instead on distance modulus μ, with odds of approximately 150:1 ($\Delta \ln (Z) = 5.03 \pm 0.03$) in favour of the isotropic model. We can repeat this comparison in the isotropic ΛCDM case and compare that with an anisotropic ΛCDM model with $F(z) = \exp (-z/S)$, finding $\Delta \ln (Z) = -4.92 \pm 0.15$, which again favours the isotropic model with odds of 136:1.

Another interesting question is the strength of evidence in favour of an accelerating universe in the isotropic expansion case. The Bayes factor between the isotropic ΛCDM model and an isotropic model with no dark energy ($\Omega_\Lambda = 0$) disfavours the latter with odds in excess of 120:1 (including selection effects corrections). For completeness (and to compare the above Bayesian model comparison results with a hypothesis testing approach), we have also computed the log-likelihood difference for the best-fitting parameter values:

$$\Delta \ln(L) = \ln \hat{L}_{\Omega_\Lambda=0} - \ln \hat{L}_{\Lambda CDM}, \qquad (49)$$

where $\hat{L}_{\Lambda CDM}$ is the maximum likelihood value for the ΛCDM model and $\hat{L}_{\Omega_\Lambda=0}$ is the maximum likelihood value for a universe with no dark energy. We find $\Delta \ln (L) = -6.35$ (with selection effects correction), which we translate into a p-value using Chernoff theorem (as the hypothesis being tested, $\Omega_\Lambda = 0$, lies on the boundary of the allowed parameter space), obtaining a p-value of 5.9×10^{-3} for the hypothesis that $\Omega_\Lambda = 0$.

In the phenomenological Cosmographic expansion setting, the accelerating isotropic model, with a uniform prior on $q_0 \in [-2, 0)$ is favoured with odds of approximately 26:1 when compared to a coasting universe, i.e. $q_0 = 0$. The accelerating universe is preferred with odds of almost $\sim 1100:1$ when compared with a decelerating model, i.e. one with a uniform prior $q_0 \in (0, 1]$.

5 SUMMARY AND CONCLUSIONS

We have revisited the question of a dipolar anisotropy in the expansion of the universe, and derived new constraints on a possible dipolar modulation from SNIa data. Our approach builds on the Bayesian hierarchical model `BAHAMAS`, which has been extended to include a new approximate correction for residual colour-based selection effects. We have also upgraded the treatment of peculiar velocities and host galaxy redshifts from the original JLA paper, by adopting state-of-the-art flow models constrained using the 2M++ galaxy catalogue. Finally, we have improved the treatment of both statistical and systematic uncertainties pertaining to peculiar velocity corrections – the dominant source of error for $z \lesssim 0.1$ SNIa, which are all-important for a robust, accurate and precise measurement of anisotropy in the local expansion.

We did not find any evidence for a deviation from isotropy, either in the framework of ΛCDM or in phenomenological Cosmographic expansion. We placed tight constraints on the amplitude of a possible dipole both in the distance modulus and on the deceleration parameter. Our upper bounds are more stringent by a factor of ~ 2 than the results previously obtained from the same data sets with a comparable approach. We note that all previous searches that have

claimed a significant detection of anisotropy have neglected peculiar velocity corrections.

We have used the framework of Bayesian model comparison to evaluate the Bayes factor between models featuring a dipole and an isotropically expanding universe (both in ΛCDM and in the Cosmographic expansion). We found moderate to strong Bayesian evidence against an anisotropic expansion. We have also evaluated the evidence in favour of acceleration, finding that a non-zero cosmological constant is preferred, using JLA SNe alone, by odds of 120:1, a result corroborated by a more traditional p-value approach based on a frequentist hypothesis test, which rejects $\Omega_\Lambda = 0$ with a p-value of 5.9×10^{-3}. In the Cosmographic expansion, a decelerating universe is disfavoured with odds of almost 1100: 1 w.r.t. an accelerating one. We conclude that the preferred model remains the ΛCDM isotropically expanding model.

Our work does not address the important question of the so-called 'H_0 tension' – the fact that the value of the Hubble–Lemaître constant obtained from local distance ladder measurements shows a highly statistical significant discrepancy with respect to the smaller value obtained via CMB anisotropies at high redshift (see e.g. Di Valentino et al. 2021 for a review). SNe type Ia, on their own, only provide a relative distance measurement, given the exact degeneracy between H_0 and M_0. However, in combination with calibrated distance indicators, such as Cepheid variables, they deliver an absolute distance scale that is used to obtain tight constraints on H_0, see Riess et al. (2021) for the latest results of the SH0ES collaboration, and Freedman (2021), who finds that calibrating SNIa via the tip of the Red Giant Branch (TRGB) instead, the tension with the CMB anisotropies-determined value is no longer significant. The novel peculiar velocity corrections presented here have potentially a bearing on this important problem, in that a change in the estimated peculiar velocity implies a horizontal shift of the SNIa in the Hubble diagram – potentially even correlated across several SNe. This in turn could affect the linear fit that gives, via the slope, the value of H_0. While we leave the investigation of this effect to future work, we do provide our new corrections to the JLA data publicly (see Data Availability section at the end), so that others wishing to use it for studies of H_0 can do so.

In this work we adopted the JLA compilation since we were unable to use the most recent Pantheon sample, owing to the full covariance matrix (including systematics) not being publicly available. We plan to apply our new framework, including up-to-date peculiar velocity corrections, to the Foundation sample (Foley et al. 2018; Jones et al. 2019), together with the recent data release of the Dark Energy Survey (Abbot et al. 2019). In the near future, we expect to be able to obtain even tighter constraints on possible anisotropy in the expansion from upcoming, larger SNIa surveys like the one that will be delivered by the Vera Rubin Observatory Legacy Survey of Space and Time (LSST) (LSST Science Collaboration 2009).

ACKNOWLEDGEMENTS

DATA AVAILABILITY

A Python implementation of BAHAMAS for public used in this article is being worked on and will be made available soon. The data products generated from our analysis from the article is available from https://zenodo.org/record/5854639.

REFERENCES

Abbot T. M. C. et al., 2019, Phys. Rev. L, 122, 171301
Akrami Y., Fantaye Y., Shafieloo A., Eriksen H. K., Hansen F. K., Banday A. J., Górski K. M., 2014, ApJ, 784, L42
Amanullah R. et al., 2010, ApJ, 716, 712
Andrade U., Bengaly C. A. P., Alcaniz J. S., Santos B., 2018a, Phys. Rev. D, 97, 083518
Andrade U., Bengaly C. A. P., Santos B., Alcaniz J. S., 2018b, ApJ, 865, 119
Antoniou I., Perivolaropoulos L., 2010, J. Cosmol. Astropart. Phys., 2010, 012
Azzalini A., Arellano-Valle R. B., 2012, preprint (arXiv:1203.2376)
Bennett C. L. et al., 2013, ApJS, 208, 20
Bernal C., Cárdenas V. H., Motta V., 2017, Phys. Lett. B, 765, 163
Betoule M. et al., 2014, A&A, 568, A22
Boruah S. S., Hudson M. J., Lavaux G., 2020, MNRAS, 498, 2703
Boruah S. S., Hudson M. J., Lavaux G., 2021, MNRAS, 507, 2697
Branchini E. et al., 1999, MNRAS, 308, 1
Brout D., Scolnic D., 2021, ApJ, 909, 26
Brout D. et al., 2022, preprint (arXiv:2202.04077)
Buchner J. et al., 2014, A&A, 564, A125
Cai R.-G., Tuo Z.-L., 2012, J. Cosmol. Astropart. Phys., 2012, 004
Calcino J., Davis T., 2017, J. Cosmol. Astropart. Phys., 2017, 038
Campanelli L., Cea P., Fogli G. L., Marrone A., 2011, Phys. Rev. D, 83, 103503
Carr A., Davis T. M., Scolnic D., Said K., Brout D., Peterson E. R., Kessler R., 2021, preprint (arXiv:2112.01471)
Carrick J., Turnbull S. J., Lavaux G., Hudson M. J., 2015, MNRAS, 450, 317
Chambers K. C. et al., 2016, preprint (arXiv:1612.05560)
Childress M. J., Wolf C., Zahid H. J., 2014, MNRAS, 445, 1898
Colin J., Mohayaee R., Rameez M., Sarkar S., 2019a, preprint (arXiv:1912.04257)
Colin J., Mohayaee R., Rameez M., Sarkar S., 2019b, A&A, 631, L13
Conley A. et al., 2011, ApJS, 192, 1
Cooke R., Lynden-Bell D., 2010, MNRAS, 401, 1409
Dam L. H., Heinesen A., Wiltshire D. L., 2017, MNRAS, 472, 835
Davis M., Nusser A., Willick J. A., 1996, ApJ, 473, 22
Davis T. M. et al., 2011, ApJ, 741 67
Di Valentino E. et al., 2021, Class. Quantum Gravity, 38, 153001
Feroz F., Hobson M. P., 2008, MNRAS, 384, 449
Feroz F., Hobson M. P., Bridges M., 2009, MNRAS, 398, 1601
Feroz F., Hobson M. P., Cameron E., Pettitt A. N., 2019, Open J. Astrophys., 2, 10
Foley R. J. et al., 2018, MNRAS, 475, 193
Freedman W. L., 2021, ApJ, 919, 16
Frieman J. A. et al., 2008, AJ, 135, 338
Gonçalves R. S., Carvalho G. C., Bengaly C. A. P., Carvalho J. C., Alcaniz J. S., 2018, MNRAS, 481, 5270
Gonçalves R. S., Carvalho G. C., Andrade U., Bengaly C. A. P., Carvalho J. C., Alcaniz J., 2021, J. Cosmol. Astropart. Phys., 2021, 029
Gupta S., Saini T. D., Laskar T., 2008, MNRAS, 388, 242
Guy J., Astier P., Nobili S., Regnault N., Pain R., 2005, A&A, 443, 781
Guy J. et al., 2007, A&A, 466, 11
Hamuy M., Phillips M. M., Maza J., Suntzeff N. B., Schommer R. A., Aviles R., 1995, AJ, 109, 1
Heneka C., Marra V., Amendola L., 2014, MNRAS, 439, 1855
Hicken M., Wood-Vasey W. M., Blondin S., Challis P., Jha S., Kelly P. L., Rest A., Kirshner R. P., 2009, ApJ, 700, 1097
Hinton S. R. et al., 2018, ApJ, 876, 15

Hollinger A. M., Hudson M. J., 2021, MNRAS, 502, 3723
Hudson M. J., 1993, MNRAS, 265, 43
Huterer D., 2020, ApJ, 904, L28
Hutsemékers D., Cabanac R., Lamy H., Sluse D., 2005, A&A, 441, 915
Hutsemékers D., Braibant L., Pelgrims V., Sluse D., 2014, A&A, 572, A18
Javanmardi B., Porciani C., Kroupa P., Pflamm-Altenburg J., 2015, ApJ, 810, 47
Jiménez J. B., Salzano V., Lazkoz R., 2015, Phys. Lett. B, 741, 168
Jones D. O. et al., 2019, ApJ, 881, 19
Kelly B. C., 2007, ApJ, 665, 1489
Kessler R., Scolnic D., 2017, ApJ, 836, 56
Kessler R. et al., 2009, ApJSS, 185, 32
Kolatt T. S., Lahav O., 2001, MNRAS, 323, 859
Kowalski M. et al., 2008, ApJ, 686, 749
Lavaux G., Hudson M. J., 2011, MNRAS, 416, 2840
Lilow R., Nusser A., 2021, MNRAS, 507, 1557
Lin H.-N., Wang S., Chang Z., Li X., 2016a, MNRAS, 456, 1881
Lin H.-N., Li X., Chang Z., 2016b, MNRAS, 460, 617
LSST Science Collaboration, 2009, preprint (arXiv:0912.0201)
Maartens R., 2011, Philos. Trans. R. Soc. Lond. Ser. A, 369, 5115
Mandel K. S., Scolnic D. M., Shariff H., Foley R. J., Kirshner R. P., 2017, ApJ, 842, 93
March M. C., Trotta R., Berkes P., Starkman G. D., Vaudrevange P. M., 2011, MNRAS, 418, 2308
Mariano A., Perivolaropoulos L., 2012, Phys. Rev. D, 86, 083517
Neill J. D., Hudson M. J., Conley A., 2007, ApJ, 661, L123
Nielsen J. T., Guffanti A., Sarkar S., 2016, Sci. Rep., 6, 35596
Perlmutter S. et al., 1997, ApJ, 483, 565
Perlmutter S. et al., 1999, ApJ, 517, 565
Phillips M. M., 1993, ApJ, 413, L105
Phillips M. M., Lira P., Suntzeff N. B., Schommer R. A., Hamuy M., Maza J., 1999, AJ, 118, 1766
Pike R. W., Hudson M. J., 2005, ApJ, 635, 11
Planck Collaboration I, 2020, A&A, 641, A1
Planck Collaboration XVI, 2016, A&A, 594, A16
Pskovskii Y. P., 1977, Sov. Astron., 21, 675
Pskovskii Y. P., 1984, Sov. Astron., 28, 658
Radburn-Smith D. J., Lucey J. R., Hudson M. J., 2004, MNRAS, 355, 1378
Riess A. G., Press W. H., Kirshner R. P., 1996, ApJ, 473, 88
Riess A. G., Davis M., Baker J., Kirshner R. P., 1997, ApJ, 488, L1
Riess A. G. et al., 1998, AJ, 116, 1009
Riess A. G. et al., 2007, ApJ, 659, 98
Riess A. G. et al., 2021, preprint(arXiv:2112.04510)
Rubin D., Hayden B., 2016, ApJ, 833, L30
Rubin D., Heitlauf J., 2020, ApJ, 894, 68
Rubin D. et al., 2015, ApJ, 813, 137
Rust B. W., 1974, PhD thesis, Oak Ridge National Lab., TN
Said K., Colless M., Magoulas C., Lucey J. R., Hudson M. J., 2020, MNRAS, 497, 1275
Sako M. et al., 2018, Publ. Astron. Soc. Pac., 130, 064002
Sarkar S., Pandey B., Khatri R., 2019, MNRAS, 483, 2453
Schwarz D. J., Weinhorst B., 2007, A&A, 474, 717
Schwarz D. J., Copi C. J., Huterer D., Starkman G. D., 2016, Class. Quantum Gravity, 33, 184001
Scolnic D. M. et al., 2018a, ApJ, 859, 101
Scolnic D. et al., 2018b, ApJ, 859, 101
Secrest N., von Hausegger S., Rameez M., Mohayaee R., Sarkar S., Colin J., 2021, ApJ, 908, L51
Shariff H., Jiao X., Trotta R., van Dyk D. A., 2016, ApJ, 827, 1
Smith M. et al., 2020, MNRAS, 494, 4426
Soltis J., Farahi A., Huterer D., Liberato C. M., 2019, Phys. Rev. Lett., 122, 091301
Stahl B. E., de Jaeger T., Boruah S. S., Zheng W., Filippenko A. V., Hudson M. J., 2021, MNRAS, 505, 2349
Strauss M. A., Willick J. A., 1995, Phys. Rep., 261, 271
Sullivan M. et al., 2010, MNRAS, 406, 782
Sullivan M. et al., 2011, ApJ, 737, 102
Sun Z. Q., Wang F. Y., 2018a, Eur. Phys. J. C, 79, 783
Sun Z. Q., Wang F. Y., 2018b, MNRAS, 478, 5153
Sun Z. Q., Wang F. Y., 2019, Eur. Phys. J. C, 79, 783
Thorp S., Mandel K. S., Jones D. O., Ward S. M., Narayan G., 2021, MNRAS, 508, 4310
Tripp R., 1998, A&A, 331, 815
Trotta R., 2008, Contemp. Phys., 49, 71
Turnbull S. J., Hudson M. J., Feldman H. A., Hicken M., Kirshner R. P., Watkins R., 2012, MNRAS, 420, 447
Visser M., 2004, Class. Quantum Gravity, 21, 2603
Wang J. S., Wang F. Y., 2014, MNRAS, 443, 1680
Yang X., Wang F. Y., Chu Z., 2014, MNRAS, 437, 1840
Zhao D., Zhou Y., Chang Z., 2019, MNRAS, 486, 5679
Zheng C. et al., 2008, AJ, 135, 1766

APPENDIX A: DERIVATION AND TEST OF METHOD OF MOMENTS

We present here the derivation of the first and second moment of the moments generating function. We also demonstrate that our method of moments correctly recovers the selection function from simulations and that inference from replica of the data under the model is unbiased.

Consider the distribution of the random variable C, denoting the observed colour within a single survey and redshift bin sj. From equations (29) and (30), we wish to compute the moment generating function

$$M_C(t) = \int_{-\infty}^{\infty} e^{t\hat{c}} f_C(\hat{c}) \mathrm{d}\hat{c} \tag{A1}$$

$$= \frac{1}{p(I = 1|\Psi, \Theta)}$$
$$\times \int_{-\infty}^{\infty} e^{t\hat{c}} \cdot \frac{1}{\sqrt{2\pi\sigma^2}} e^{-\frac{1}{2\sigma^2}(\hat{c}-c_\star)^2} \cdot \Phi\left(\frac{c_{sj}^{\mathrm{obs}} - \hat{c}}{\sigma_{sj}^{\mathrm{obs}}}\right) \mathrm{d}\hat{c}, \tag{A2}$$

where $\sigma^2 \equiv R_c^2 + \sigma_{\hat{c}}^2$, and $\sigma_{\hat{c}}$ is the average measurement noise for colour observations (which we approximate as being the same for all data points in a given survey and redshift bin).

The above can be recast as:

$$M_C(t) = \frac{e^{c_\star t + \frac{1}{2}\sigma^2 t^2}}{p(I = 1|\Psi, \Theta)}$$
$$\times \int_{-\infty}^{\infty} \frac{1}{\sqrt{2\pi\sigma^2}} e^{-\frac{1}{2\sigma^2}(\hat{c}-(c_\star+\sigma^2 t))^2} \Phi\left(\frac{c_{sj}^{\mathrm{obs}} - \hat{c}}{\sigma_{sj}^{\mathrm{obs}}}\right) \mathrm{d}\hat{c} \tag{A3}$$

$$= \frac{e^{c_\star t + \frac{1}{2}\sigma^2 t^2}}{p(I = 1|\Psi, \Theta)} \int_{-\infty}^{\infty} \mathcal{N}_{\hat{c}}(c_\star + \sigma^2 t, \sigma^2) \cdot \Phi\left(\frac{c_{sj}^{\mathrm{obs}} - \hat{c}}{\sigma_{sj}^{\mathrm{obs}}}\right) \mathrm{d}\hat{c} \tag{A4}$$

$$= \frac{e^{c_\star t + \frac{1}{2}\sigma^2 t^2}}{p(I = 1|\Psi, \Theta)} \Phi\left(\frac{c_{sj}^{\mathrm{obs}} - (c_\star + \sigma^2 t)}{\sqrt{\sigma^2 + \sigma_{sj}^{\mathrm{obs}2}}}\right). \tag{A5}$$

We now compute the first and second moments, set $h(t) \equiv e^{c_\star t + \frac{1}{2}\sigma^2 t^2}$ and $g(t) = \frac{c_{sj}^{\mathrm{obs}} - (c_\star + \sigma^2 t)}{\sqrt{\sigma^2 + \sigma_{sj}^{\mathrm{obs}2}}}$. A dash ($'$) symbol indicates a derivative with respect to t. Hence:

$$\left.\frac{\mathrm{d}M_C(t)}{\mathrm{d}t}\right|_{t=0} = \frac{1}{p(I = 1|\Psi, \Theta)} \frac{\mathrm{d}}{\mathrm{d}t}\left[h(t)\Phi(g(t))\right]_{t=0}$$
$$= \frac{1}{p(I = 1|\Psi, \Theta)}\left[h'(t)\Phi(g(t)) + h(t)\Phi'(g(t))\right]_{t=0} \tag{A6}$$

and

$$\frac{\mathrm{d}^2 M_{C(t)}}{\mathrm{d}t^2}\bigg|_{t=0} = \frac{1}{p(I_i = 1|\Psi, \Theta)}\left[h''(t)\Phi(g(t)) + 2h'(t)\Phi'((g(t)) + h(t)\Phi''(g(t))\right]_{t=0} \tag{A7}$$

We derive each of the terms $h(t)$, $h'(t)$, $h''(t)$, $\Phi(g(t))$, $\Phi'(g(t))$, and $\Phi''(g(t))$ evaluated at $t = 0$:

$$h(0) = 1. \tag{A8}$$

$$h'(0) = h(t)(c_\star + \sigma^2 t)|_{t=0} = c_\star. \tag{A9}$$

$$h''(0) = h(t)\sigma^2 + h'(t)(c_\star + \sigma^2 t)|_{t=0} = \sigma^2 + c_\star^2. \tag{A10}$$

To determine $\Phi'(g(t))$ and $\Phi''(g(t))$ we use the Leibniz rule for differentiating under an integral (the CDF). As a reminder, our CDF is from the integral of $\mathcal{N}_x(0, 1)$ from $-\infty$ up to $g(t)$ with c_{sj}^{obs} and $\sigma_{sj}^{\mathrm{obs}}$ used to control the width as opposed to the normal distribution hyperparameters. This gives:

$$\Phi(g(t = 0)) = \int_{-\infty}^{g(0)} \frac{1}{\sqrt{2\pi}}.e^{-\frac{1}{2}x^2}\mathrm{d}x \tag{A11}$$

$$\Phi'(g(t = 0))| = \frac{\mathrm{d}}{\mathrm{d}t}\left[\int_{-\infty}^{g(t)} \frac{1}{\sqrt{2\pi}}.e^{-\frac{1}{2}x^2}\mathrm{d}x\right]_{t=0} \tag{A12}$$

$$= \frac{1}{\sqrt{2\pi}}.e^{-\frac{1}{2}g(t)^2}.g'(t)|_{t=0} \tag{A13}$$

$$= -\frac{\sigma^2}{\sqrt{2\pi}\sqrt{\sigma^2 + \sigma_{sj}^{\mathrm{obs}2}}}e^{-\frac{1}{2}\frac{(c_{sj}^{\mathrm{obs}}-c_\star)^2}{\sigma^2+\sigma_{sj}^{\mathrm{obs}2}}} \tag{A14}$$

where $g(0) = \frac{c_{sj}^{\mathrm{obs}}-c_\star}{\sqrt{\sigma^2+\sigma_{sj}^{\mathrm{obs}2}}}$ and $g'(t)|_{t=0} = -\frac{\sigma^2}{\sqrt{\sigma^2+\sigma_{sj}^{\mathrm{obs}2}}}|_{t=0} = -\frac{\sigma^2}{\sqrt{\sigma^2+\sigma_{sj}^{\mathrm{obs}2}}}$. Finally,

$$\Phi''(t = 0) = \frac{1}{\sqrt{2\pi}}.e^{-\frac{1}{2}g(t)^2}. - g(t).g'^2(t)$$
$$+ \frac{1}{\sqrt{2\pi}}.e^{-\frac{1}{2}g(t)^2}g''(t)|_{t=0} \tag{A15}$$

$$= \frac{1}{\sqrt{2\pi}}.e^{-\frac{1}{2}g(t)^2}(g''(t) - g(t)g'^2(t))\bigg|_{t=0}. \tag{A16}$$

Given that, $g''(t)|_{t=0} = 0$, this reduces to

$$\Phi''(g(t))|_{t=0} = -\frac{1}{\sqrt{2\pi}}.e^{-\frac{1}{2}g(0)^2}(g(0)g'^2(0)). \tag{A17}$$

This leads to the first and second moments:

$$\frac{\mathrm{d}M_C(t)}{\mathrm{d}t}\bigg|_{t=0} = \frac{1}{p(I = 1|\Psi, \Theta)}$$
$$\times \left(c_\star\Phi(g(0)) - \frac{\sigma^2}{\sqrt{2\pi}\sqrt{\sigma^2 + \sigma_{sj}^{\mathrm{obs}2}}}e^{-\frac{1}{2}\frac{(c_{sj}^{\mathrm{obs}}-c_\star)^2}{\sigma^2+\sigma_{sj}^{\mathrm{obs}2}}}\right), \tag{A18}$$

$$\frac{\mathrm{d}^2 M_C(t)}{\mathrm{d}t^2}\bigg|_{t=0} = \frac{1}{p(I = 1|\Psi, \Theta)}$$
$$\times \Bigg((\sigma^2 + c_\star^2)\Phi(g(0))$$
$$- \frac{2c_\star\sigma^2}{\sqrt{2\pi}\sqrt{\sigma^2 + \sigma_{sj}^{\mathrm{obs}2}}}e^{-\frac{1}{2}\frac{(c_{sj}^{\mathrm{obs}}-c_\star)^2}{\sigma^2+\sigma_{sj}^{\mathrm{obs}2}}}$$
$$- \frac{\sigma^4}{\sqrt{2\pi}}e^{-\frac{1}{2}\left(\frac{(c_{sj}^{\mathrm{obs}}-c_\star)^2}{\sigma^2+\sigma_{sj}^{\mathrm{obs}2}}\right)}\left(\frac{c_{sj}^{\mathrm{obs}} - c_\star}{(\sigma^2 + \sigma_{sj}^{\mathrm{obs}2})^{3/2}}\right),\Bigg) \tag{A19}$$

where the normalization constant is given by equation (28).

We tested our method of moments to reconstruct the selection function on a suite of simulations, with $c_\star = 0.0$, $R_c = 0.1$, and three different choices of selection function parameters: $\{c_{sj}^{\mathrm{obs}}, \sigma_{sj}^{\mathrm{obs}}\} = \{[-0, 1, 0.02], [-0.1, 0.10], [0.0, 0.06]\}$, chosen the span the parameter space of interest in our application. We show the results of the reconstructed selection function for $N_{sj} = 30$, 50, 200 (from top to bottom) in Fig. A1. The results show that the reconstruction, when averaged over realizations, is extremely close to the underlying true selection function, thus validating the method.

We tested parameter inference in the presence of residual colour-based selection effects data simulated according to the method presented in Section 3.1, with colour-based selection effects as described in Section 2.4, with selection function parameters for each survey being:

SDSS = $\{(-0.5, 3.4), (-0.5, 0.57), (-0.35, 0.29), (0.20, 0.20), (0.20, 0.20)\}$,

SNLS = $\{(0.20, 0.20), (-0.50, 1.17), (0.14, 0.17), (-0.06, 0.13), (-0.18, 0.14)\}$,

Low-z = $\{(-0.50, 2.95), (-0.50, 4.47), (0.09, 0.01), (0.017, 0.01)\}$,

HST = $\{(-0.01, 0.12)\}$, where each tuple gives the values of $(c_{sj}^{\mathrm{obs}}, \sigma_{sj}^{\mathrm{obs}})$ in order from lowest redshift bin to highest within each survey. In the reconstruction, we estimate the selection function parameters as described above, and present 1D and 2D marginal posteriors on all parameters in Fig. A2. The posterior distributions have been averaged over $N = 100$ replicas. We observe that the posterior for all of the parameters has a mode very close to the true value, thus validating our methodology.
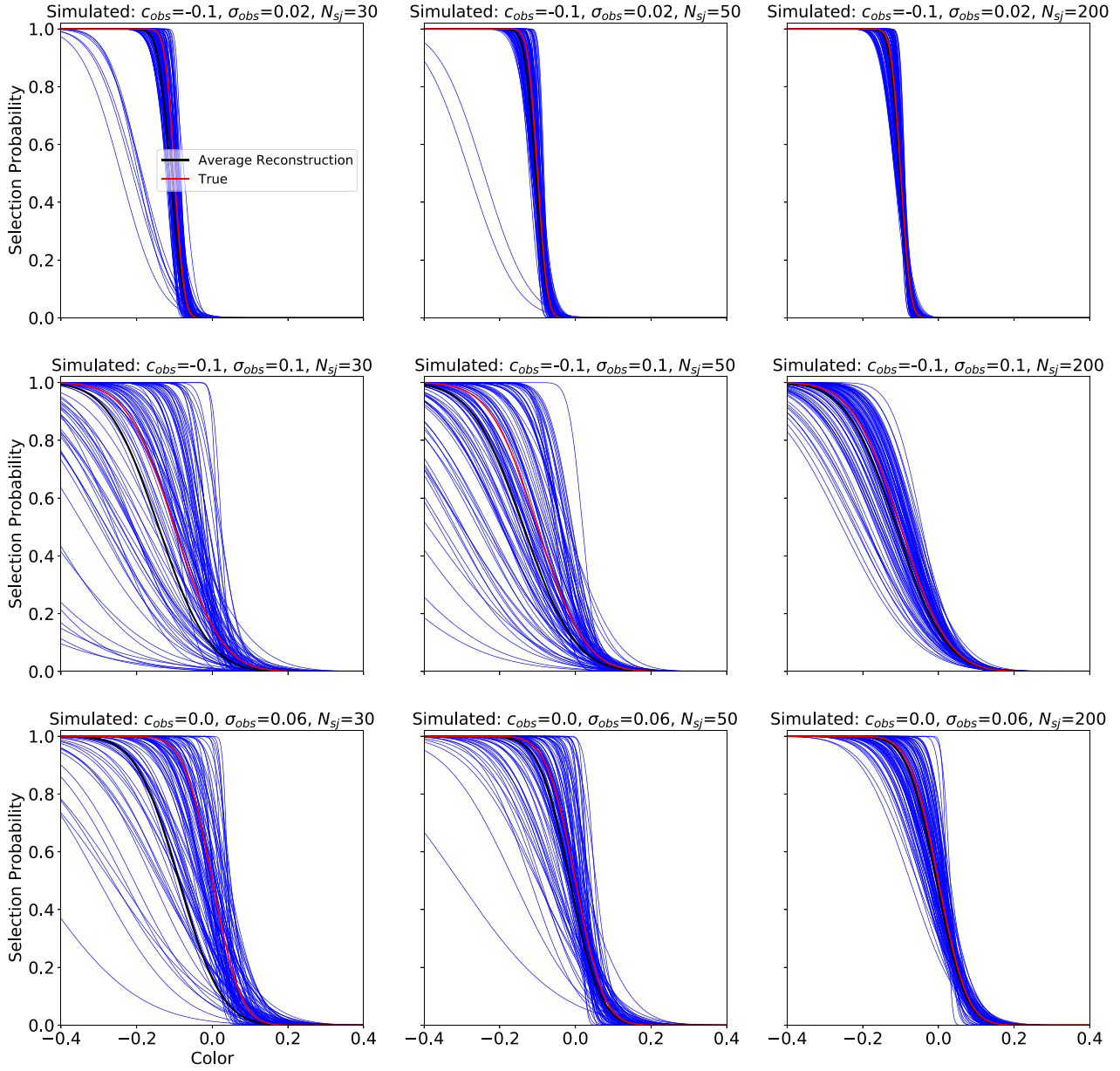
Figure A1. Reconstructions of the selection function from the two first moments of the moment generating function from simulated data: we show three representative choices for the selection function parameters, c_{sj}^{obs}, σ_{sj}^{obs} (columns) and three different sample sizes (SNe per bin, $N_{sj} = 30, 50, 100$, top to bottom in rows). Blue lines are the individual reconstruction from each of $N_{sim} = 100$ simulations; dashed green is the mean reconstruction averaged over realizations, and solid red is the true selection function.
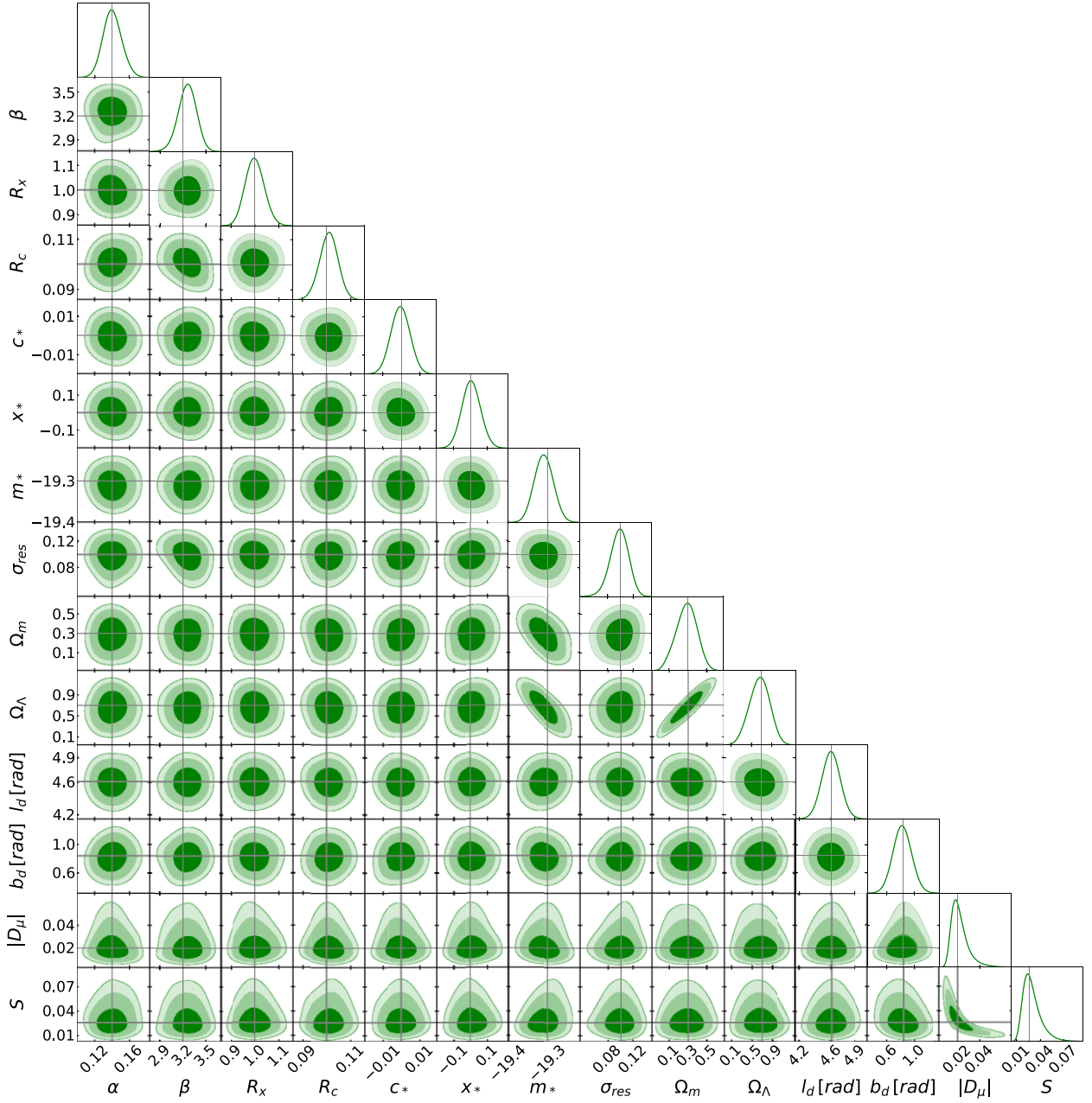
Figure A2. Posterior marginal distributions on simulated data with colour-based selection effects, and a simulated dipole, averaged over $N = 100$ data realizations. The posterior includes a correction for colour-based selection effects according to our method. Vertical lines give the true value of the parameters.

This paper has been typeset from a TEX/LATEX file prepared by the author.